Science of the Total Environment 1014 (2026) 181261

Contents lists available at ScienceDirect

Science of the Total Environment

journal homepage: www.elsevier.com/locate/scitotenv

# Multi-decadal geodetic mass balance, climate sensitivity, and projected glacier response in the Chandra–Bhaga Basin, Western Indian Himalaya (1971–2100)

Atanu Bhattacharya [a,b,*], Ankita Paul [a], Kriti Mukherjee [c,*], Julekha Khatun [a], Sajid Ghuffar [d], Tobias Bolch [e]

[a] Department of Earth Sciences & Remote Sensing, JIS University, Kolkata, India
[b] Centre for Data Science, JIS Institute of Advanced Studies & Research, Kolkata, India
[c] Cranfield Environment Centre, Cranfield University, Bedford, UK
[d] Department of Space Science, Institute of Space Technology, Islamabad, Pakistan
[e] Institute of Geodesy, Graz University of Technology, Graz, Austria

## HIGHLIGHTS

- Glaciers in Chandra–Bhaga Basin lost 0.26 ± 0.10 m w.e. $a^{-1}$ since the 1970s.
- Summer temperature has most significant control on glacier mass budget.
- Rising temperature and declining winter precipitation accelerated mass loss.
- Up to 70 % glacier volume may be lost by 2100 even under a low emission scenario.
- Small glaciers (area < 0.5 $km^2$) may disappear before mid-century.

## GRAPHICAL ABSTRACT

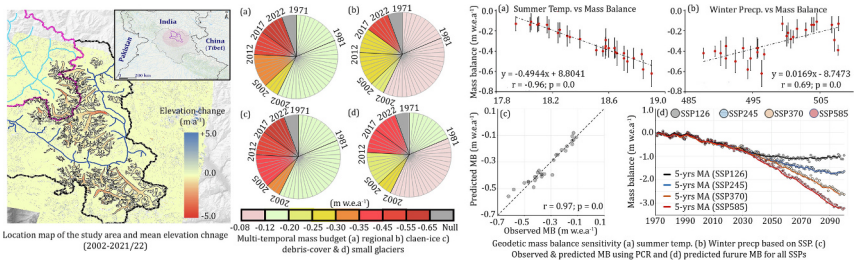


## ARTICLE INFO

*Keywords:*
Glacier mass balance
Climate sensitivity
High Mountain Asia (HMA)
Remote sensing
Future projections (SSP scenarios)

## ABSTRACT

Glaciers in the Chandra–Bhaga basin, western Indian Himalaya, are critical to the cryosphere–hydrosphere system, yet their long-term climate responses remain poorly understood due to sparse in-situ data. Our geodetic mass balance assessment reveal substantial ice loss from 1971 to 2022, with glaciers shrinking by 0.72 ± 0.08 $km^2$ $a^{-1}$ and losing mass at 0.26 ± 0.10 m w.e. $a^{-1}$. Debris-covered glaciers experienced greater ice loss (0.28 ± 0.10 m w.e. $a^{-1}$) than clean-ice glaciers (0.20 ± 0.12 m w.e. $a^{-1}$). CMIP6-based regression indicates modest pre-2000 loss, then average loss rates of −0.5 m w.e. $a^{-1}$ until ~2035, after which trajectories diverge depending on SSP scenarios. Temperature sensitivity is strongest in summer (−0.49 m w.e. $a^{-1}$ °$C^{-1}$) and weakest in winter (−0.38 m w.e. $a^{-1}$ °$C^{-1}$). Precipitation sensitivity is highest for winter and lowest for summer. ERA5 Land reanalysis-based sensitivities show annual temperature has stronger influence than seasonal, with lower magnitudes than CMIP6. Winter precipitation from ERA5 Land reanalysis data show stronger correlation to glacier mass gain compared to CMIP6. These differences emphasize uncertainty over which dataset better represents regional climate, particularly for temperature–mass balance relationships and winter precipitation that largely governs glacier accumulation. Despite this, sensitivities align with broader Himalayan trends. Projections suggest stable winter precipitation, combined with increased summer and annual warming, will accelerate mass loss through the 21st century. This study proves that long-term geodetic data can provide an alternative solution to

* Corresponding authors.
*E-mail addresses:* atanudeq@gmail.com (A. Bhattacharya), kriti.mukherjee@cranfield.ac.uk (K. Mukherjee).

https://doi.org/10.1016/j.scitotenv.2025.181261
Received 19 August 2025; Received in revised form 14 December 2025; Accepted 16 December 2025
Available online 15 January 2026
0048-9697/© 2025 The Authors. Published by Elsevier B.V. This is an open access article under the CC BY license (http://creativecommons.org/licenses/by/4.0/).

understand glacier–climate interactions in data-scarce regions such as the Himalaya, enabling reconstructions, forecasts, and targeted adaptation for glacier-dependent communities.

## 1. Introduction

Under a changing climate, most of the glaciers worldwide have been losing mass at an accelerated rate in the last decades (GlaMBIE Team, 2025) and projected increase in global temperatures raises concerns about the sustainability of the Alpine cryosphere (Hock et al., 2019; Rounce et al., 2023). Reflecting global trends, glaciers in High Mountain Asia (HMA), which hosts a substantial number of glaciers (~138,000) covering an area of approximately 102,100 $km^2$ (RGI v7.0, Consortium, 2023), are increasingly at risk of long-term sustainability. Meltwater from this high-altitude water tower influences the streamflow of major Asian rivers, impacting downstream agriculture, hydropower, and municipal needs particularly during dry seasons (Immerzeel et al., 2020). Furthermore, intensified glacier melting significantly influences ongoing natural hazards, contributes to global sea-level rise, and alters the regional hydrological cycle (Bolch et al., 2012; GlaMBIE Team, 2025).

However, glacier responses are notably more complex and heterogeneous across spatial and temporal scales (Bhattacharya et al., 2021; Hugonnet et al., 2021). This heterogeneity is further influenced by morpho-topographical factors and the presence of supra and proglacial lakes (Bhattacharya et al., 2023). Enhanced mass loss has also accelerated glacier lake formation and increased GLOF-related risks to downstream communities (Allen et al., 2019).

Building on these observations, the sensitivity of regional glacier mass balances to key climate drivers, combined with the influence of projected climate change, provides important insights into future glacier evolution and its implications for hydrological systems (Hock and Huss, 2021). Model-based surface mass balance approaches are commonly used to assess climate-driven glacier sensitivity, though such approaches rely heavily on glaciological mass balance data which is only available for less than 1 % of the glaciers across the world (WGMS, 2024). Despite the high concentration of glaciers in the Himalayan region, long-term in-situ observations remain limited due to logistical and geopolitical challenges (Bolch et al., 2012). To bridge this knowledge gap, long-term satellite-based glacier mass balance estimates are essential for assessing regional variability. In this context, the availability of declassified satellite data is a valuable input to reconstruct extended glacier mass balance time series for periods when modern satellite stereo imagery was unavailable (Bolch et al., 2011; Maurer et al., 2019).

Across the diverse climatic regimes of the Indian Himalayas, the Chandra-Bhaga basin in Lahaul-Spiti, western Indian Himalaya, holds climatic significance as a transitional zone influenced by both winter westerlies and summer monsoon circulation (Tawde et al., 2017). Previous studies have reported substantial glacier mass loss in this region, ranging from −0.36 to −0.65 m w.e. $a^{-1}$ since around 2000 (Vijay and Braun, 2016; Mukherjee et al., 2018). However, these observations are limited to just one or two extended periods. Most of the available long-term glacier mass balance data and climate sensitivity in the Indian Himalaya are mostly confined to individual glaciers, with the Chhota Shigri Glacier being the only glacier maintaining an uninterrupted annual surface mass balance record exceeding 20 years (Azam et al., 2024; WGMS, 2024). However, spatially resolved multi-temporal datasets at the regional scale remain scarce, limiting our ability to capture the heterogeneous glacier responses and to understand the broader glacier–climate interactions across the Himalaya.

Bhattacharya et al. (2023) established a relationship between long-term regional geodetic mass balance and individual climate drivers, such as seasonal temperature and precipitation, in the nearby Alaknanda Basin. However, an integrated analysis that examines glacier mass balance sensitivity to combined climate drivers and projects future mass changes has not yet been explored.

Therefore, in this study we investigate the long-term, multi-temporal variability of regional glacier mass balance and develop a relationship between mass balance and combined climate variables to assess the sensitivity to ongoing climate change in the Chandra-Bhaga basin, Lahaul-Spiti, western Indian Himalaya. We also project future regional glacier mass changes under multiple Shared Socioeconomic Pathway (SSP) scenarios. The specific objectives of this study are:

- Developing a comprehensive multi-decadal (1971–2022) geodetic glacier mass balance record.
- Linking geodetic glacier mass balance with climate variables to reconstruct past and project future mass balance.
- Assessing mass balance sensitivity to individual climate parameters to identify the dominant controls.

## 2. Study region

The study region is located in the Chandra-Bhaga Basin within the Lahaul-Spiti region of the western Himalaya, in Himachal Pradesh, India, encompassing approximately 32.07°N–32.72°N latitude and 77.08°E–77.79°E longitude (see Fig. 1). Spanning a total area of ~4113 $km^2$, the basin contains a glacierized extent of about 1060 $km^2$, accounting for roughly 26 % of the study region. The Chandra and Bhaga sub-basins host approximately 370 and 320 glaciers, covering ~568 $km^2$ and ~ 370 $km^2$ of glacierized area, respectively. Elevation in the Chandra Basin ranges from 1800 to 6600 m above sea level (asl.), while in the Bhaga Basin it varies between 2860 and 6460 m asl. (Tawde et al., 2017). Two major rivers, the Chandra (~131 km) and the Bhaga (~80 km), traverse this region, serving as critical freshwater sources for the downstream areas.

Glaciers in the Chandra-Bhaga Basin are influenced by dual climatic systems: the Indian summer monsoon in summer and the midlatitude westerlies during winter (Azam et al., 2024). Accumulation predominantly occurs in the form of snowfall during the winter months from October to April (Azam et al., 2024). Meteorological records from the Bhuntar observatory, located approximately 50 km from the Chhota Shigri Glacier at an elevation of 1084 m asl, indicate a near-balanced seasonal precipitation pattern, with summer and winter contributing 42 % and 40 % of the annual total, respectively. For the present study, a total of 348 glaciers were analyzed, of which 82 are located in the Bhaga Basin, while the remaining 266 are distributed across the Chandra Basin and its surrounding regions (Fig. 1).

## 3. Dataset

We used a variety of satellite images and auxiliary data for the analysis (Table 1, for detailed information we refer to Supplementary Table T1). We used the glacier outlines based on the Randolph Glacier Inventory 7.0 (RGI v7.0, Consortium, 2023), as the basis for our glacier inventory.

### 3.1. Satellite data

We analyzed glacier length/area and mass changes from 1971 to 2022 using optical satellite stereo images with resolutions ranging from 1.8 m to 15 m. Declassified stereo products like Corona (KH-4B) and Hexagon (KH-9) panoramic camera, along with SPOT-5 and ASTER-L1A, were used for regional glacier monitoring. Additionally, freely available Pleiades DEMs (2 m spatial resolution) from the Pléiades Glacier Observatory (PGO) initiative by the French Space Agency (CNES) and

LEGOS, France (Berthier et al., 2024) and Cartosat-1 (2.5 m) stereo products supported detailed analyses of 10 specific glaciers (Fig. 1). Additionally, we used an open-source Digital Elevation Model (DEM) of 30 m spatial resolution (NASA DEM) for raw stereo images processing.

### 3.2. Climate data

We used Coupled Model Intercomparison Project Phase 6 (CMIP6) ensemble mean data (Eyring et al., 2016) for monthly near-surface air temperature and precipitation across four SSPs (SSP126, SSP245, SSP370, SSP585) to calibrate a mass balance model and project future glacier mass balance. SSPs employed in CMIP6 provide an integrated framework that combines socioeconomic narratives with updated climate forcings, enabling more comprehensive and realistic glacier change projections (Eyring et al., 2016). Moreover, the use of bias-corrected monthly temperature and precipitation data from an ensemble of thirteen CMIP6 climate models under the SSP framework offers improved spatial resolution and a more accurate representation of key climate processes, enhancing the reliability of glacier mass balance estimations (Eyring et al., 2016). Additionally, we also used temperature and precipitation data (1971–2022) from nearby Bhuntar observatory at monthly temporal resolution to compare the CMIP6 temperature and precipitation trend during the observation period. ERA5 Land reanalysis climate data (Muñoz-Sabater et al., 2021) was used to estimate regional geodetic mass balance sensitivity and to compare the variations with CMIP6 climate data derived sensitivity.

### 3.3. Mass balance data

We generated a comprehensive set of 21 multi-temporal glacier mass balance data by employing various combinations of DEM pairs. These DEM pairs allowed us to compute 21 glacier elevation change grids covering various time intervals from 1971 to 2022, which in turn facilitated the estimation of glacier mass balance through geodetic methods. To enhance the robustness and temporal coverage of our analysis, we supplemented our datasets with seven additional mass balance estimates obtained from existing literature: five decadal and multi-decadal estimates (for the periods 2000–2005, 2005–2010, 2010–2015, 2015–2020, and the cumulative 2000–2020) from Hugonnet et al. (2021); one estimate covering 2000–2016 from Brun et al. (2017); and one long-term estimate from 1975 to 2000 reported by Maurer et al. (2019). This aggregation resulted in a total of 28 glacier mass balance observations, each representing a distinct time interval.

### 3.4. Ancillary data

The Randolph Glacier Inventory (RGI v7.0, Consortium, 2023) was used as a baseline, and multi-temporal inventories were created using orthoimages from the DEM sources and Landsat ETM+/OLI data. We also incorporated global debris thickness data (Rounce et al., 2021) to identify debris-covered glaciers and ice thickness maps (Farinotti et al., 2019) to analyze the glacier mass balance response in changing climate.

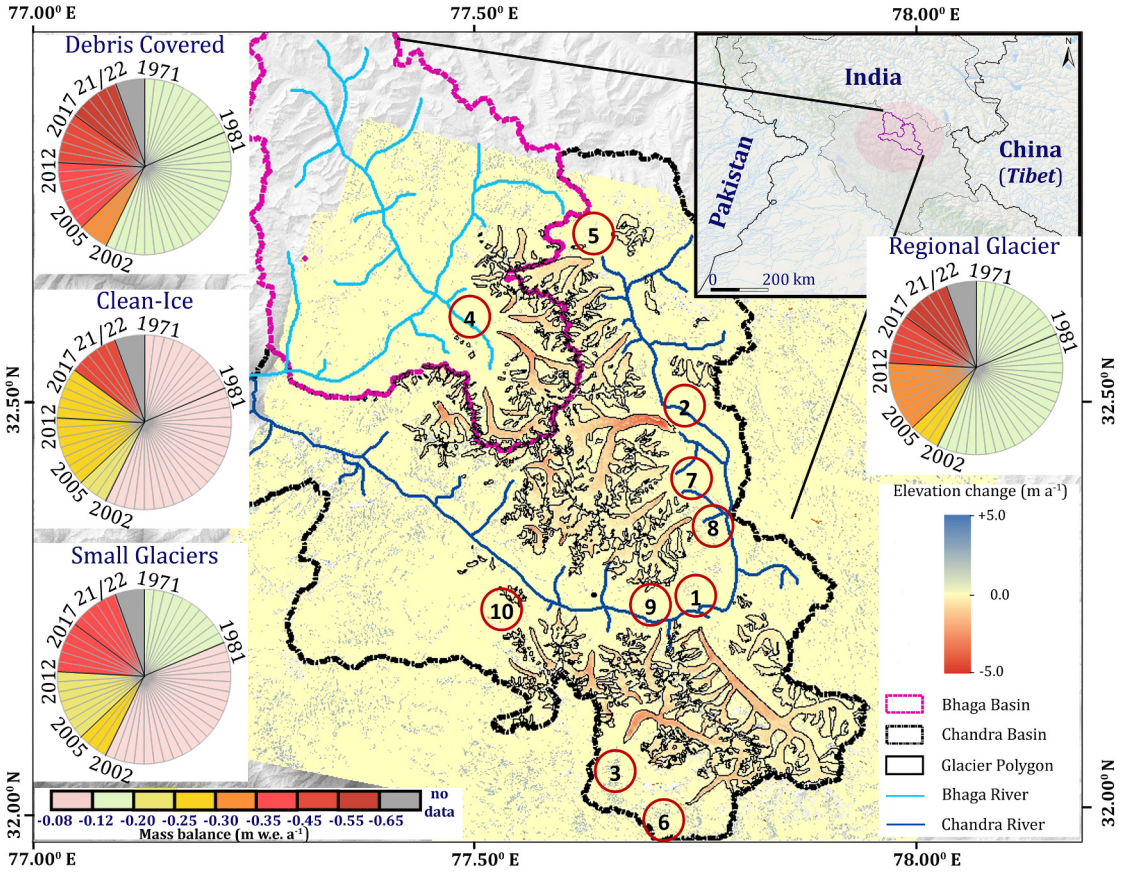


**Fig. 1.** Location map of the study area and mean glacier surface elevation changes for 2002 to 2021/22. Ten representative glaciers were selected for detailed analysis [1: Bara Shigri (RGI2000-v7.0-G-14-32,495); 2: Samudra Tapu (RGI2000-v7.0-G-14-30,345); 3: RGI2000-v7.0-G-14-30,407; 4: Mulkila (RGI2000-v7.0-G-14-30,161); 5: RGI2000-v7.0-G-14-32,569; 6: RGI2000-v7.0-G-14-30,491; 7: Sutri-Dhaka (RGI2000-v7.0-G-14-32,508); 8: Batal (RGI2000-v7.0-G-14-32,505); 9: Chhota Shigri (RGI2000-v7.0-G-14-30,579); 10: Hamtah (RGI2000-v7.0-G-14-30,385)]. Multi-temporal mass balance estimates (in m w.e. $a^{-1}$) of overall, debris covered, clean-ice and small glacier are in the accompanying pie diagrams.

**Table 1**
Brief information about the satellite images and other data used in this study.

| Sensors | Spatial resolution (m) | Date of acquisition | Usages |
|---|---|---|---|
| Corona KH-4B | 1.8 | 28-09-1971 | Glacier mapping & Mass balance |
| Hexagon KH-9 PC | 0.6–1.2 | 21-08-1980 & 10-07-1982 | Glacier mapping & Mass balance |
| SPOT-5 | 2.5–5.0 | 26-11-2002 & 22-12-2002 | Glacier mapping & Mass balance |
| ASTER | 15 | 29-10-2005; 07-11-2005; 25-10-2012; 01-11-2012; 21-09-2017; 14-10-2017; 30-10-2017; 19-12-2021 & 05-10-2022 | Glacier mapping & Mass balance |
| Cartosat-1 | 2.5 | 19-10-2011; 02-11-2012; 04-10-2014; 16-10-2014 | Glacier mapping & Mass balance |
| Pléiades 1B DEM | 2.0 | 26-09-2014 & 12-09-2020 | Glacier Mass balance |
| Landsat 7 ETM+ | 15 | 02-12-2000 | Glacier mapping |
| Landsat 8 OLI | 15 | 30-10-2020 | Glacier mapping |
| NASADEM V001 | 30 | 11-02-2000 | Orto-rectification |
| CMIP6 | – | 1971–2100 | Climate analysis |
| ERA5 Land Reanalysis | 10 km | 1971–2022 | Climate analysis |
| Weather Station (Bhuntar) | – | 1971–2022 | Climate analysis |
| Randolph Glacier Inventory | | RGI7.0 | Glacier Mapping |

## 4. Methods

### 4.1. Glacier mapping and associated uncertainty

The debris-covered regions of the identified glaciers (Rounce et al., 2021) were delineated manually using the slope gradient and curvature information derived from corresponding DEMs and shaded relief was also used to visually inspect and manually adjust the glacier boundaries. The clean-ice glaciers were adjusted by using the band ratio of near infrared to short wave infrared (NIR/SWIR) of the available multi spectral optical data. We could hardly identify changes in accumulation areas on the utilised medium to high resolution images. As the changes are typically minor above the median elevations, we kept the upper glacier area constant and only adjusted the parts below the median elevations. We have analyzed length fluctuation of the individual glaciers along the lines drawn parallel (every 50 m distance) to the main flow direction. The length change uncertainty ($U$) was estimated using the method proposed by Hall et al. (2003) as follows

$$U = \sqrt{(r_1)^2 + (r_2)^2} + \sigma_{NMAD} \quad \text{(i)}$$

Where $U$ is the length change uncertainty, $r_1$ and $r_2$ refers to the spatial resolution of the first image and second image respectively. $\sigma_{NMAD}$ refers to the coregistration error.

We accounted for mapping inaccuracies in glacier area estimation by applying a ± 2 % uncertainty for debris-free glaciers (Bolch et al., 2010), and an additional ± 0.5 % for debris-covered glaciers due to the difficulty in visually identifying debris-covered tongues (Bolch et al., 2010). Image coregistration uncertainty was included using -a buffer with buffer widths set to twice the root-mean-square error (RMSE) of mapping and digitizing errors. Estimated RMSEs were 7.2 m (4 pixels) for Corona KH-4B, 7.2 m (6 pixels) for Hexagon-KH9, 10 m (2 pixels) for SPOT-5, 7.5 m (0.5 pixels) for ASTER-L1A, 7.5 m (3 pixels) for Cartosat-1, and 7.5 m (0.5 pixels) for Landsat 7/8 outlines. We also considered another error component (3 % for clean ice and debris cover individually) due to scene quality, clouds, seasonal snow and shadow (Bolch et al., 2010). Overall area change uncertainty was calculated using the law of error propagation.

### 4.2. Generation of DEMs from stereo satellite data

We generated all DEMs in this study using photogrammetric methods via various software platforms and automated pipelines.

#### 4.2.1. DEMs from declassified data

Older panchromatic declassified satellite images (Corona KH-4 and Hexagon KH-9) have lower contrast; therefore, we enhanced the contrast prior to DEM generation by using a local adaptive filtering along with histogram equalization.

The Corona KH-4 DEMs were generated using the Remote Sensing Software Graz (RSG) version 22.0.7, developed by Joanneum Research Graz. We employed a corona-adopted distortion model which was based on a modified collinearity equation. Initially, the panoramic camera's orientation parameters were determined using ground control points (GCPs) taken from Landsat 7 ETM+ panchromatic images in combination with elevation data from the NASA DEM. Then we co-registered stereo image pairs using RSG's automated tie point measurement tool, which utilizes the Förstner operator for identifying suitable points. Before applying epipolar registration, we employed a polynomial rectification technique to reduce parallax error (Bhattacharya et al., 2021). Following this, disparity matching was performed in three stages employing variable search windows. These window sizes were iteratively refined to improve the accuracy of pixel matching. Finally, we generated DEMs at 10-m spatial resolution using area resampling techniques.

To reconstruct complete image scenes from the KH9 Panoramic Camera, we first mosaicked individual image strips by identifying and aligning overlapping areas using tie points (Ghuffar et al., 2023). We used the Corona Stereo Pipeline (CoSP) framework (Ghuffar et al., 2022) for remaining processing. We used SuperGlue deep learning model (Ghuffar et al., 2022) for point matching between KH9 imagery and Landsat 7 ETM+ panchromatic reference images. The matched image points, in combination with elevation data from the NASA DEM, were used to extract ground control points (GCPs), which supported the estimation and refinement of camera orientation through bundle adjustment (Ghuffar et al., 2023). We used epipolar resampling to ensure geometric alignment of stereo image pairs, followed by dense image matching using the semi-global matching (SGM) algorithm to generate a high-density 3D point cloud via triangulation. To accurately geolocate this 3D dataset, a tile-based coregistration was carried out using a least-squares surface matching technique. Finally, the adjusted point cloud was interpolated into a raster-format DEM at a 10-m spatial resolution. The overall workflow for generating DEMs from declassified KH-4 and KH-9 data, along with the key processing parameters, is summarized in Fig. 2 (a-b) to provide a clearer overview of the procedure.

#### 4.2.2. DEMs from stereo pairs acquired after 2000

We used AMES Stereo Pipeline (ASP, v3.1.0), a software suite originally developed by NASA and subsequently enhanced by Shean et al. (2016) to generate DEMs for stereo images (ASTER Level-1 A, SPOT5, Cartosat-1 and Pleiades 1B) acquired after 2000. We used an external DEM (1 arc-second NASA DEM) for initial orthorectification of the stereo images. We used semi-global matching (SGM) algorithm with a 7 × 7-pixel correlation window (Shean et al., 2016) for matching stereo pairs. To mitigate artifacts in the resulting disparity images we used SGM disparity map filters (Shean et al., 2016). Valid disparity pixels were further refined using a Bayesian Expectation-Maximization (Bayes EM) weighted affine adaptive window correlator. We carried out stereo triangulation by using a rational polynomial coefficient (RPC) sensor

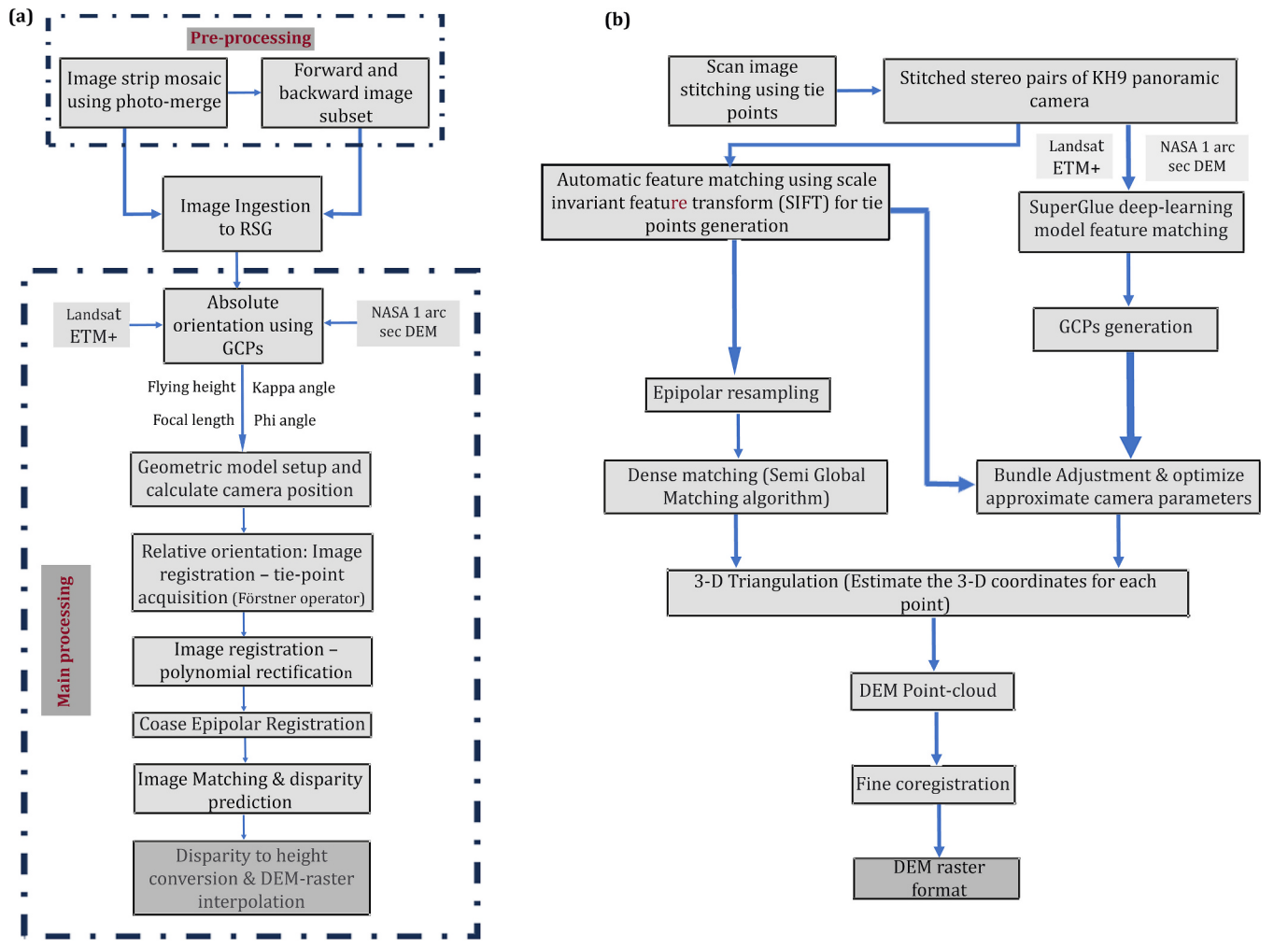


**Fig. 2.** The overall workflow for generating DEMs from (a) declassified KH-4 and (b) KH-9 data, along with the key processing parameters (modified after Ghuffar et al., 2022).

model. Finally, we produced DEMs of 30 m, 10 m, 5 m and 2 m spatial resolution for ASTER, SPOT5, Cartosat-1 and Pleiades respectively in the WGS84 ellipsoidal coordinate system.

### 4.3. Geodetic mass balance and uncertainty estimation

We coregistered DEMs from various stereo sources with the void-filled 30 m NASA DEM using methods by Nuth and Kääb (2011). We estimated and removed elevation-dependent biases due to the tilt for each dataset using two-dimensional first-order polynomial trend surfaces (Hugonnet et al., 2021). We applied a two-step filtering process to remove outliers from the elevation difference (dH) grids over glaciated regions: first, pixels with dH values beyond ±150 m were excluded; second, a three-cell buffer around data gaps was used to remove high-magnitude dH values (Falaschi et al., 2023). Regional elevation differences were then estimated in 50 m altitude bins using pixels within μ ± 3σ (μ = mean and σ =standard deviation within the elevation bin), following Gardelle et al. (2013).

Due to low contrast in the accumulation zones of Corona KH-4 and Hexagon KH-9, we applied an elevation-dependent sigmoid function to model the non-linear glacier thickness change, constraining maximum change in the ablation zone and minimum in the accumulation zone (Pieczonka and Bolch, 2015). In the first step, we normalized each glacier pixel's elevation (N) while taking its maximum elevation range into account as follows

$$N = \frac{Max_e - Min_e}{Glac_e} \quad \text{(ii)}$$

where, $N$ is the normalized glacier elevation in each pixel; $Max_e$ and $Min_e$ are the maximum and minimum elevation for the whole region respectively and $Glac_e$ is the glacier elevation of the pixel in meter.

We then estimated the maximum allowable thickness change ($\Delta h_{max}$) for any pixel in a specific region as follows:

$$\Delta h_{max} = [5 - 5\tanh(2\pi - 5N)] \times \sigma_g \quad \text{(iii)}$$

where, $\sigma_g$ is the overall standard deviation of the glacier elevation differences.

To fill the data gaps in the resulting elevation change grid, we used global mean hypsometric approach (McNabb et al., 2019) by fitting a third order polynomial function to the mean elevation change on 50 m elevation bins. Finally, the volume changes were converted into mass changes by considering the average ice density of 850 ± 60 kg $m^{-3}$ (Huss, 2013).

We estimated geodetic mass balance uncertainty by extracting pixels over stable terrain. Overall glacier mass balance uncertainty ($\sigma_{mb}$) was calculated using the method by Brun et al. (2017) by considering (i) uncertainty in elevation change ($\sigma_{\Delta H}$), (ii) uncertainty associated in glacier area ($\sigma_e$) estimation and (iii) uncertainty associated in volume to mass conversion.

First, we estimated surface elevation changes uncertainty ($\sigma_{\Delta H}$) as

described by Rolstad et al. (2009) as follows

$$\sigma_{\Delta H} = \sqrt{\sigma_{\Delta h}^2 \times \frac{A_{cor}}{5 \times GA_i}} \quad \text{(iv)}$$

where, $\sigma_{\Delta h}^2$ is the variance of elevation change estimates over stable terrain in meter, $A_{cor}$ is the area over which elevation change data are correlated, which was estimated as $A_{cor} = \pi \times L^2$, where, $L$ is the auto-correlation length (500 m, Brun et al., 2017) and $GA_i$ is the glacier area at the beginning of our observation period for each DEM pair.

Next, we estimated uncertainty associated with glacier area/volume change ($\sigma_{\Delta v}$) according to Brun et al. (2017) as follows by considering data void which varies from 11.7 % to 37.1 % in different combinations of elevation difference girds.

$$\sigma_{\Delta v} = \sqrt{[\sigma_{\Delta H}\{DP_i + 5 \times (1 - DP_i)\} \times GA_i]^2 + [\sigma_e \times dh]^2} \quad \text{(v)}$$

Where $DP_i$ is the fraction of glacier area having valid elevation difference values after outlier removal, $\sigma_e$ is uncertainty associated with glacier area which was considered as 10 % of the initial glacier area (0.1 × $GA_i$) as mentioned by Kääb et al. (2012). $dh$ is the mean rate of elevation change in the glacierized area from the corresponding DEMs.

Finally, the overall uncertainty was obtained by using the following Eq. (vi)

$$\sigma_{mb} = \sqrt{(\sigma_{\Delta v} \times \rho_{V1})^2 + (\sigma_{\rho V1} \times \Delta v)^2} \quad \text{(vi)}$$

Where $\rho_{V1}$ is the volume to mass conversion factor (850 kg $m^{-3}$) and $\sigma_{\rho V1}$ is the uncertainty of the volume to mass conversion factor (60 kg $m^{-3}$) by Huss (2013). $\Delta v$ is the volume change. A summary of glacier area and geodetic mass balance uncertainties is provided in the supplementary materials (Supplementary Table T2).

### 4.4. Development of mass balance model for future projection and sensitivity analysis

We extracted six key climatic variables, as predictor variables, from the SSP dataset to develop a relationship of climate with geodetic mass balance observations. These included mean summer (May–September), winter (October–April), and annual temperature, and precipitation. The climate variables were computed as averages across all available SSP scenarios to generalize the climatic trends across different future emission trajectories.

In climatic datasets, high multicollinearity among predictor variables, such as seasonal and annual temperature and precipitation, is common and can significantly compromise the reliability of standard multiple linear regression by inflating the variance of coefficient estimates, making them unstable and difficult to interpret. To mitigate this issue, we applied Principal Component Analysis (PCA), which transforms the original correlated variables into a new set of uncorrelated variables known as principal components (PCs).

To achieve this, we first standardized all predictor variables to have zero mean and unit variance to ensure comparability and remove scale-related biases. Then we performed principal component transformation on this standardized set. We plotted the cumulative explained variance against the number of principal components and applied the elbow method to determine the optimal number of PCs to retain. The selected components together accounted for over 95 % of the total variance, beyond which additional components added negligible information.

Each principal component represents a weighted linear combination of the original standardized variables, including summer, winter, and annual temperature and precipitation. We have calculated the loading vectors to the selected PCs, which quantify contribution of each predictor variable in a given PC. Using the retained PCs, we developed a Principal Component Regression (PCR) model to predict glacier mass balance based on 28 mass balance observation data. Finally, for interpretability, we subsequently projected the regression coefficients from the PC space back into the original climate variable space, enabling a clearer understanding of how each variable contributes to mass balance variability.

Model performance was evaluated using standard statistical metrics such as the Root Mean Squared Error (RMSE) and the coefficient of determination ($R^2$). To further assess model robustness and its ability to generalize across independent data subsets, we employed Leave-One-Out Cross-Validation (LOOCV).

To project future glacier mass balance under varying climate change scenarios, we compiled seasonal and annual climate projections (temperature and precipitation) for each future year across different SSPs. These projected climatic variables were then input into our trained regression model to estimate glacier mass balance under each future scenario, allowing for an assessment of potential glacier responses to different climate pathways.

Finally, to calculate the mass balance sensitivities to temperature ($\beta_T$) and precipitation ($\beta_P$), linear regression was performed between mass balance and each climate parameter. This approach allowed us to isolate and quantify the influence of each seasonal and annual temperature and precipitation variable on glacier mass balance and relative sensitivity of mass balance to individual climate components. According to the definitions of mass balance sensitivity (Oerlemans et al., 1998) the temperature sensitivity represents the average change in mass balance for 1 °C change in temperature. This can be directly computed from the slopes of the regression lines. The precipitation sensitivity is defined as the change in mass balance for a 10 % change in average precipitation. We also estimated regional glacier mass balance sensitivity using ERA5 Land reanalysis data and compared the results with those derived from CMIP6 climate data.

## 5. Results

### 5.1. Glacier area and length changes

The area of 348 glaciers in the Chandra-Bhaga Basin decreased by 36.5 ± 3.9 $km^2$ from 1971 to 2022, shrinking from 798.9 ± 54.2 $km^2$ to 762.4 ± 61.9 $km^2$, which represents a 4.6 ± 0.5 % (0.09 ± 0.01 % $a^{-1}$) reduction in total glacier area (Table 2; for more details we refer to Supplementary Table T3-T4). The loss accelerated after 2002, averaging 1.05 ± 0.13 $km^2$ $a^{-1}$ or 2.7 ± 0.3 % during 2002–2022, compared to 0.50 ± 0.6 $km^2$ $a^{-1}$ or 1.9 ± 0.2 % in 1971–2002. Debris-covered glaciers lost more area (23.5 ± 1.7 $km^2$) than clean-ice glaciers (13.1 ± 1.0 $km^2$) over the full period, though clean-ice glaciers experienced a higher percentage loss (11.3 ± 0.9 % vs 3.4 ± 0.2 %). The small glaciers' (<0.5 $km^2$) area also reduced significantly from 42.1 ± 4.2 $km^2$ to 37.7 ± 5.1 $km^2$ (10.5 ± 1.7 %) during the entire observation period.

Length and area change analysis for 10 individual glaciers over 1971–2002 and 2002–2022 revealed that Samudra Tapu Glacier (RGI2000-v7.0-G-14-30,345) had the highest area loss (0.05 ± 0.01 $km^2$ $a^{-1}$) and retreat rate (33.4 ± 1.01 m $a^{-1}$), likely due to the expansion of its proglacial lake (0.24 ± 0.02 $km^2$ in 1971 to 1.69 ± 0.05 $km^2$ in 2022). Chhota Shigri Glacier (RGI2000-v7.0-G-14-30,579) lost 0.01 ± 0.00 $km^2$ $a^{-1}$ and retreated at 5.7 ± 1.01 m $a^{-1}$. Bara Shigri Glacier (RGI2000-v7.0-G-14-32,495) showed a significant retreat of 28.4 ± 1.01 m $a^{-1}$ over the entire period, with the highest fluctuation (38.6 ± 0.97 m $a^{-1}$) during 1971–2002. Other selected glaciers showed variable retreat rates ranging from 5.7 ± 1.01 m $a^{-1}$ to 33.4 ± 1.01 m $a^{-1}$ over the observation period (Table 2; Supplementary Table T3-T4).

### 5.2. Multi-temporal geodetic mass balance of the regional and individual glaciers

Glaciers in the study region experienced significant mass loss of 0.26 ± 0.10 m w.e. $a^{-1}$ over the entire period 1971–2022 (Figs. 3 & 4;

**Table 2**
Mass balance, glacierised area and length change of regional and individual glaciers (RG: Regional Glacier; DCG: Debris Covered Glacier; CIG: Clean Ice Glacier and SG: Small Glacier).

Geodetic mass balance and area across the study region in different time periods

| Time period | Mass Budget (m w.e.a$^{-1}$) RG (348) | DCG (119) | CIG (229) | SG (< 0.5km$^2$) | Year | Total Glacier Area (km$^2$) RG (348) | DCG (119) | CIG (229) | SG (< 0.5 km$^2$) |
|---|---|---|---|---|---|---|---|---|---|
| 71–81 | −0.13 ± 0.07 | −0.13 ± 0.09 | −0.09 ± 0.09 | −0.12 ± 0.15 | 1971 | 798.9 ± 54.2 | 682.7 ± 34.9 | 116.2 ± 5.2 | 42.1 ± 4.2 |
| 81–02 | −0.13 ± 0.07 | −0.13 ± 0.08 | −0.13 ± 0.09 | −0.13 ± 0.08 | 1981 | 791.6 ± 53.1 | 677.8 ± 35.1 | 113.9 ± 4.9 | 41.4 ± 3.9 |
| 02–05 | −0.29 ± 0.11 | −0.31 ± 0.12 | −0.19 ± 0.17 | −0.29 ± 0.18 | 2002 | 783.4 ± 68.3 | 672.1 ± 41.1 | 111.3 ± 6.9 | 40.4 ± 4.7 |
| 05–12 | −0.35 ± 0.09 | −0.36 ± 0.09 | −0.32 ± 0.11 | −0.37 ± 0.16 | 2005 | 782.3 ± 66.5 | 671.5 ± 38.9 | 110.8 ± 6.9 | 40.3 ± 5.5 |
| 12–17 | −0.46 ± 0.10 | −0.50 ± 0.11 | −0.23 ± 0.13 | −0.48 ± 0.17 | 2012 | 779.6 ± 74.9 | 670.1 ± 37.3 | 109.5 ± 8.6 | 39.8 ± 5.6 |
| 17–22 | −0.62 ± 0.13 | −0.64 ± 0.15 | −0.54 ± 0.18 | −0.63 ± 0.18 | 2017 | 769.3 ± 60.1 | 661.6 ± 30.7 | 107.8 ± 6.8 | 38.5 ± 5.8 |
| 71–22 | −0.26 ± 0.10 | −0.28 ± 0.10 | −0.20 ± 0.12 | −0.28 ± 0.11 | 2022 | 762.4 ± 61.9 | 659.2 ± 33.1 | 103.2 ± 6.6 | 37.7 ± 5.1 |

**Individual glacier area (km$^2$), length change (LC) (m a$^{-1}$) and mass balance (MB) (m w.e.a$^{-1}$)**

| Sl. No. | Glacier Area 1971 | 2022 | LC (71–22) | MB 71–81 | MB 02–05 | MB 05–12 | MB 12–17 | MB 17–22 | MB 71–22 |
|---|---|---|---|---|---|---|---|---|---|
| 1 | 113.13 ± 0.87 | 112.31 ± 2.16 | 28.4 ± 1.01 | −0.10 ± 0.10 | −0.09 ± 0.14 | −0.33 ± 0.15 | −0.47 ± 0.16 | −0.72 ± 0.15 | −0.26 ± 0.13 |
| 2 | 82.12 ± 0.53 | 79.82 ± 1.32 | 33.4 ± 1.01 | −0.15 ± 0.12 | −0.27 ± 0.12 | −0.39 ± 0.15 | −0.64 ± 0.18 | −0.68 ± 0.12 | −0.31 ± 0.16 |
| 3 | 35.58 ± 0.33 | 34.18 ± 0.83 | 16.6 ± 1.01 | −0.10 ± 0.12 | −0.59 ± 0.17 | −0.48 ± 0.16 | −0.71 ± 0.17 | −0.92 ± 0.17 | −0.35 ± 0.14 |
| 4 | 30.01 ± 0.26 | 29.47 ± 0.65 | 18.6 ± 1.01 | −0.13 ± 0.10 | −0.32 ± 0.11 | −0.59 ± 0.17 | −0.65 ± 0.17 | −0.55 ± 0.13 | −0.29 ± 0.11 |
| 5 | 26.55 ± 0.18 | 25.38 ± 0.45 | 19.1 ± 1.01 | −0.20 ± 0.12 | −0.23 ± 0.10 | −0.43 ± 0.14 | −0.26 ± 0.14 | −0.75 ± 0.17 | −0.25 ± 0.14 |
| 6 | 25.65 ± 0.32 | 25.22 ± 0.77 | 12.8 ± 1.01 | −0.13 ± 0.12 | −0.35 ± 0.11 | −0.71 ± 0.12 | −0.53 ± 0.16 | −0.62 ± 0.17 | −0.32 ± 0.14 |
| 7 | 23.97 ± 0.19 | 22.92 ± 0.48 | 21.1 ± 1.01 | −0.06 ± 0.11 | −0.29 ± 0.13 | −0.37 ± 0.19 | −0.19 ± 0.14 | −0.39 ± 0.12 | −0.27 ± 0.13 |
| 8 | 20.74 ± 0.18 | 19.77 ± 0.4 | 23.4 ± 1.01 | −0.01 ± 0.12 | −0.21 ± 0.12 | −0.26 ± 0.15 | −0.20 ± 0.13 | −0.59 ± 0.12 | −0.22 ± 0.16 |
| 9 | 13.52 ± 0.15 | 13.27 ± 0.37 | 5.70 ± 1.01 | −0.05 ± 0.11 | −0.30 ± 0.13 | −0.32 ± 0.13 | −0.47 ± 0.16 | −0.69 ± 0.14 | −0.33 ± 0.13 |
| 10 | 4.18 ± 0.14 | 3.41 ± 0.12 | 25.1 ± 1.01 | −0.26 ± 0.12 | −0.46 ± 0.12 | −0.55 ± 0.15 | −0.73 ± 0.16 | −0.80 ± 0.17 | −0.44 ± 0.14 |

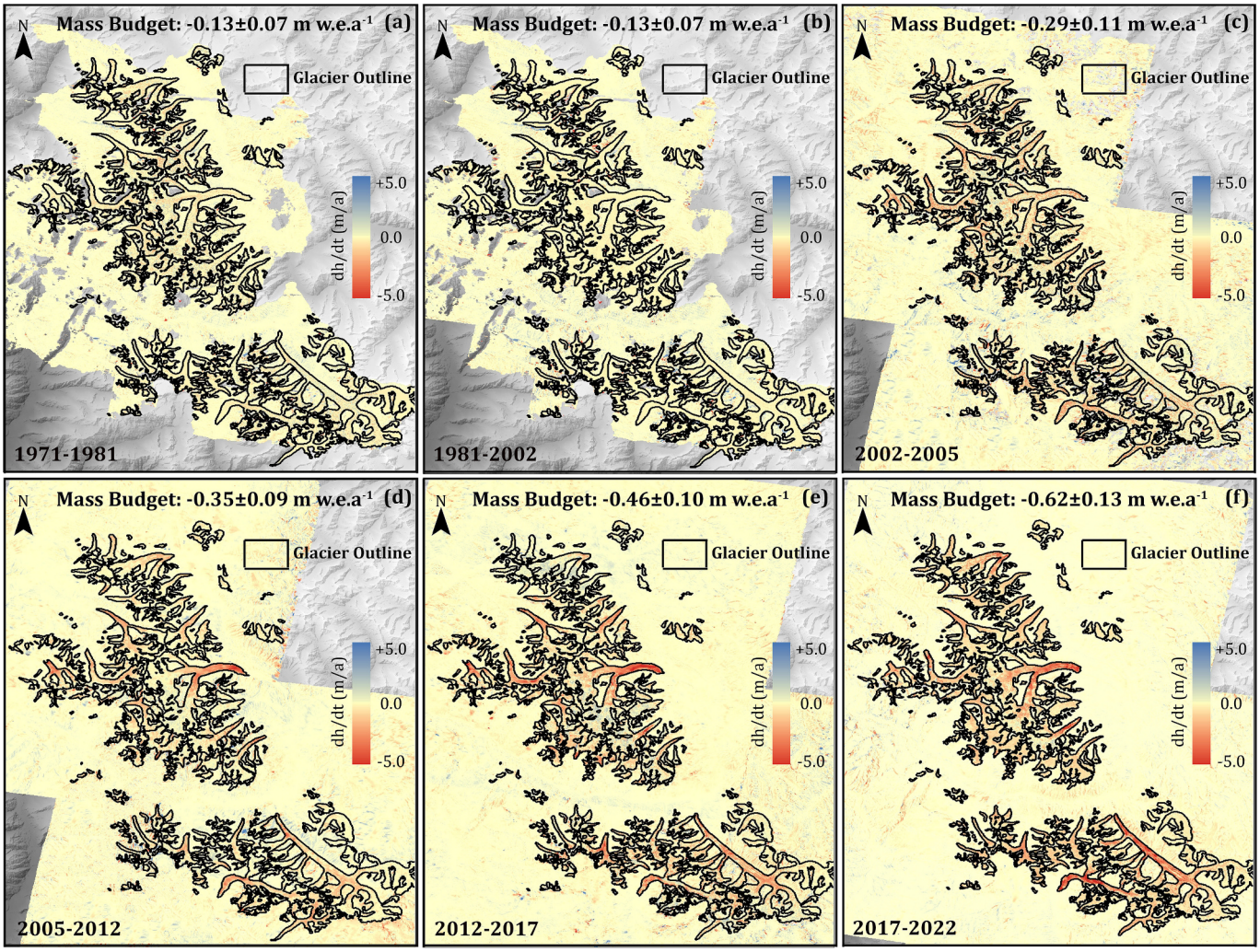


**Fig. 3.** Multi-temporal glacier elevation change rate of the study region for the periods of (a) 1971–1981; (b) 1981–2002; (c) 2002–2005; (d) 2005–2012; (e) 2012–2017 and (f) 2017–2022.

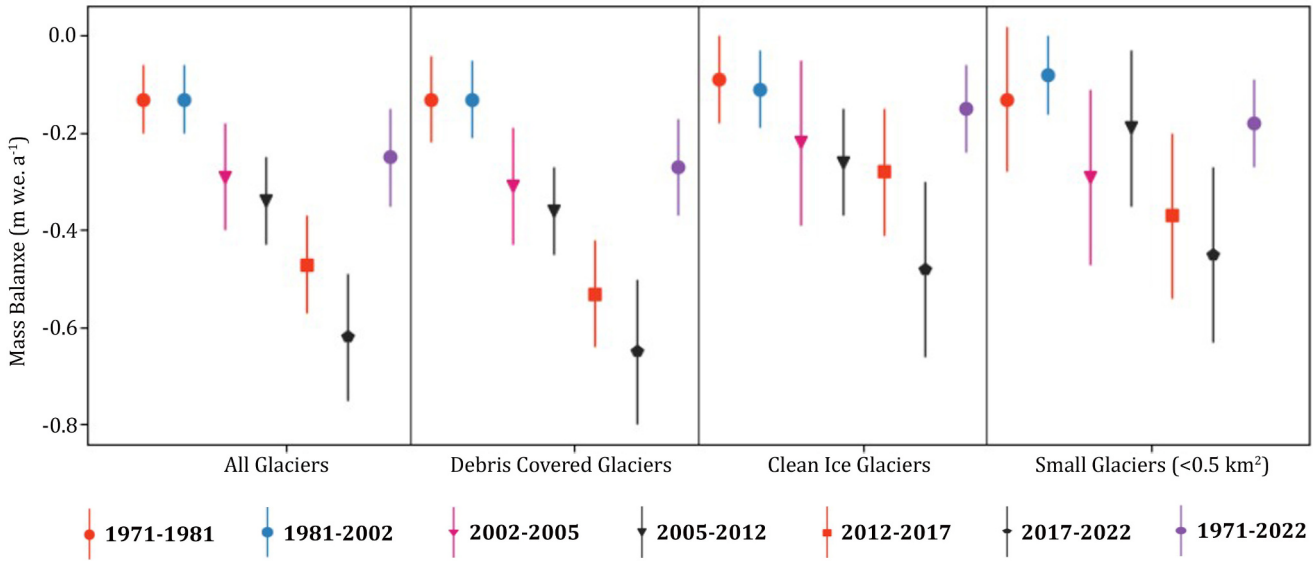


**Fig. 4.** Temporal mass balance for entire study region, debris-covered glaciers; clean-ice glaciers and small glaciers (< 0.5 km$^2$).

Table 2). Over 85 % of this thinning occurred between 3700 and 5000 m asl, with maximum thinning (~60 m) on glacier tongues below ~4150 m asl. The mass loss rate increased notably after 2000: from 0.11 ± 0.08 m w.e. a$^{-1}$ during 1971–2002 to 0.47 ± 0.12 m w.e. a$^{-1}$ in 2002–2022 (Supplementary Table T5). Debris-covered glaciers exhibited an ice loss rate at 0.28 ± 0.10 m w.e. a$^{-1}$, approximately 29 % more than that of

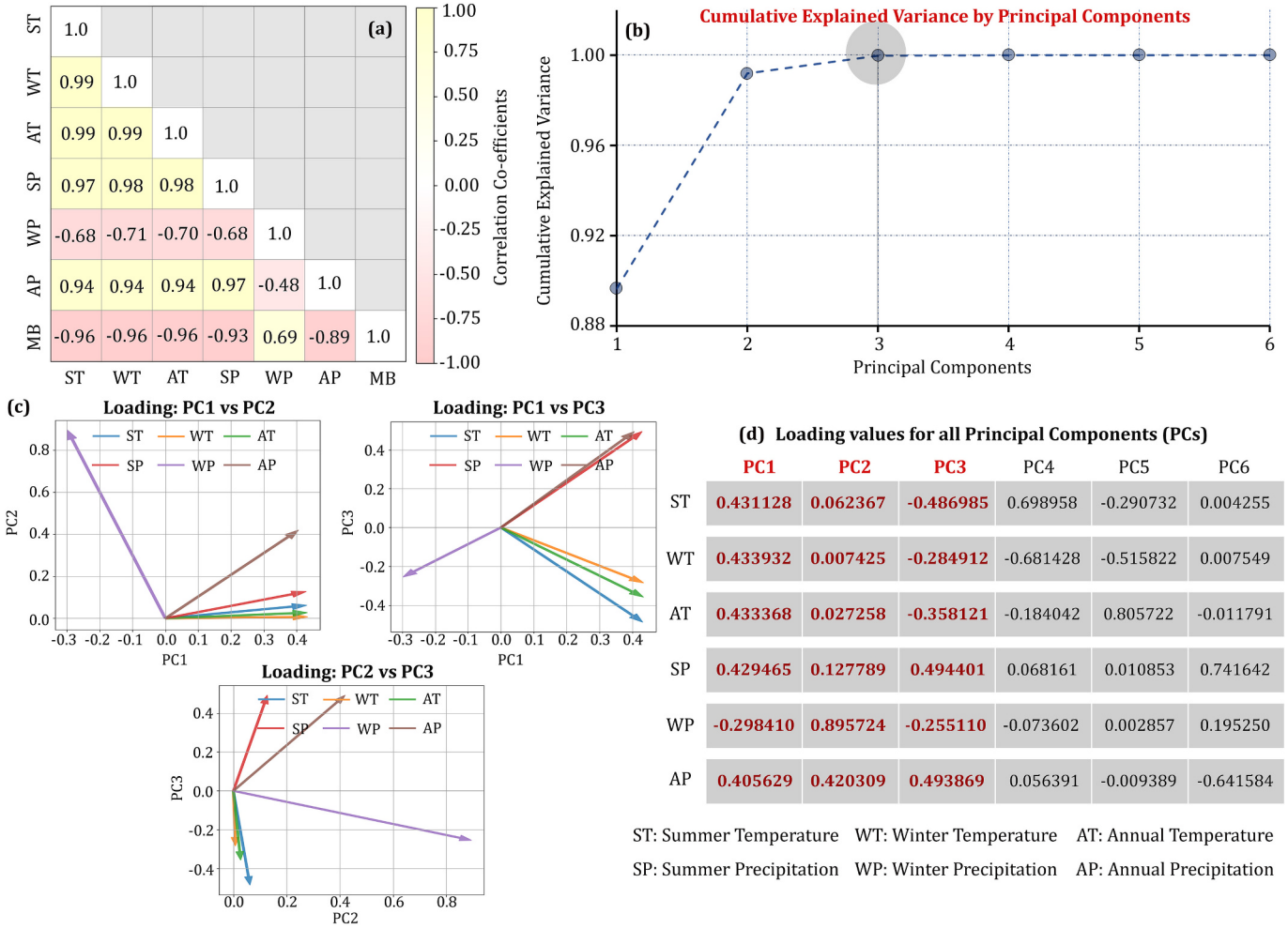


(d) Loading values for all Principal Components (PCs)

| | PC1 | PC2 | PC3 | PC4 | PC5 | PC6 |
|---|---|---|---|---|---|---|
| ST | 0.431128 | 0.062367 | -0.486985 | 0.698958 | -0.290732 | 0.004255 |
| WT | 0.433932 | 0.007425 | -0.284912 | -0.681428 | -0.515822 | 0.007549 |
| AT | 0.433368 | 0.027258 | -0.358121 | -0.184042 | 0.805722 | -0.011791 |
| SP | 0.429465 | 0.127789 | 0.494401 | 0.068161 | 0.010853 | 0.741642 |
| WP | -0.298410 | 0.895724 | -0.255110 | -0.073602 | 0.002857 | 0.195250 |
| AP | 0.405629 | 0.420309 | 0.493869 | 0.056391 | -0.009389 | -0.641584 |

ST: Summer Temperature WT: Winter Temperature AT: Annual Temperature
SP: Summer Precipitation WP: Winter Precipitation AP: Annual Precipitation

**Fig. 5.** (a) correlation coefficient matrix of the mass balance (MB) and other climate parameters from the average SSPs scenarios; (b) Explained variables vs principal components; (c) Loading vectors for all 3 selected principal components and (d) Loading values for all principal components.

clean-ice glaciers (0.20 ± 0.12 m w.e. $a^{-1}$) over the entire study period (Fig. 4; Table 2). Debris-covered parts of glaciers showed even greater surface lowering: 0.86 ± 0.17 m $a^{-1}$ on average, with 0.33 ± 0.13 m $a^{-1}$ during 1971–2002 and 1.41 ± 0.21 m $a^{-1}$ in 2002–2022. Smaller glaciers (< 0.5 $km^2$), covering ~5.3 % of the glacierized area, lost slightly more mass (0.28 ± 0.11 m w.e. $a^{-1}$) than the regional average- and their mass loss increased from 0.14 ± 0.09 m w.e. $a^{-1}$ during 1971–2002 to 0.48 ± 0.11 m w.e. $a^{-1}$ in 2002–2022. Overall, results confirm continuous mass loss in the region, with accelerated thinning after 2002 (Table 2; Supplementary Table T5).

Ten individual glaciers exhibited heterogeneous mass balances with debris cover ranging from 55.7 % to 7.2 % (Rounce et al., 2021). Hamtah Glacier (RGI2000-v7.0-G-14-30,385, 55.7 % debris) showed the highest loss (0.44 ± 0.14 m w.e. $a^{-1}$), while RGI2000-v7.0-G-14-32,505 (7.2 % debris) had the lowest loss (0.22 ± 0.16 m w.e. $a^{-1}$) during 1971–2022 (Supplementary Table T5). Between 2014 and 2020, Chhota Shigri (RGI50–14.15990) and Hamtah glaciers lost mass at 0.62 ± 0.16 m w.e. $a^{-1}$ and 0.75 ± 0.18 m w.e. $a^{-1}$, respectively, based on high-resolution Pleiades stereo data. During 1971–1981, similar to Chhota Shigri (−0.05 ± 0.11 m w.e. $a^{-1}$), RGI2000-v7.0-G-14-32,508 (−0.06 ± 0.11 m w.e. $a^{-1}$) and RGI2000-v7.0-G-14-32,505 (−0.01 ± 0.12 m w.e. $a^{-1}$) were also nearly in balance (Supplementary Table T5).

A summary of regional glacier mass balance and area change is presented in Table 2, with more detailed estimates of mass balance and area/length changes for regional and individual glaciers available in Supplementary Table T3-T5.

### 5.3. Mass balance model

#### 5.3.1. Selection of Principal Components (PCs)

We observed strong multicollinearity among the climate variables (Fig. 5a). Most of the predictor variables showed a strong negative correlation with the glacier mass budget (r ranging from −0.89 to −0.96), with the exception of winter precipitation, which exhibited a moderate positive correlation ($r$ = 0.69). Furthermore, the intercorrelations among the predictor variables themselves were highly positive, ranging from 0.94 to 0.99. However, winter precipitation showed moderate to strong negative correlations with the other predictor variables, with r values ranging from −0.48 to −0.71.

To develop a predictive mass balance equation using Principal Component Regression (PCR), we selected the first three principal components (PCs), which together explained over 95 % of the total variance in the dataset. The selection was guided not only by statistical criteria such as cumulative variance (Fig. 5b) but also by examining the loading vectors (Fig. 5c) and corresponding loading values (Fig. 5d), which allowed us to quantify the contribution of each original climate variable to the respective PCs. Importantly, the chosen PCs were also evaluated for their physical relevance and interpretability in the context of glacier–climate interactions, ensuring that the final model is both statistically robust and climatologically meaningful.

PC1 displayed moderate positive loadings (0.41 to 0.43) of summer, winter, and annual temperatures, along with summer and annual precipitation, and a negative loading (−0.30) from winter precipitation. This component reflects an overall regional climatic effect, dominated by rising temperatures and enhanced summer precipitation.

PC2 exhibited a strong positive loading for winter precipitation (0.90) and moderate contribution from annual precipitation (0.42), highlighting the role of winter snowfall as another primary contributor to glacier mass gain.

PC3 was selected as another component which likely captures interannual variability in monsoon strength. The positive loadings on summer precipitation (0.49) and annual precipitation (0.49) suggesting that higher PC3 scores are linked to increased monsoonal and overall precipitation. The negative loadings on summer (−0.48), winter (−0.28), and annual (−0.35) temperatures indicate that wetter years tend to coincide with cooler conditions across seasons. The comparatively small negative loading on winter precipitation (−0.25) suggests that this variable varies less in phase with the other loadings in PC3. Given the regional climate, this may reflect the influence of westerly disturbances, which contribute to winter precipitation independently of monsoonal variability. Therefore, This PC suggests a strong climatic contrast between cool, wet monsoonal conditions and warm, dry periods, a pattern typical of a transitional Himalayan zone influenced by both Indian summer monsoon and western disturbances.

#### 5.3.2. Projected mass balance using principal component regression (PCR) model

Based on three selected PCs, the regression model achieved a RMSE of 0.037 and $R^2$ of 0.93. Additionally, based on LOOCV we found $R^2$ = 0.88 and RMSE = 0.040. Since these RMSEs are lower than the observed uncertainty range of the geodetic mass balance estimates (0.05 to 0.13 m w.e. $a^{-1}$), the model was deemed suitable for future mass balance predictions. We plotted the estimated mass balance by the model vs the observed mass balance values (Fig. 6a) using the above equation for all 28 mass balance periods and found an excellent correlation ($r$ = 0.97, $p$ = 0.0) between them.

The final mass balance (MB) regression equation derived from the PCR model is presented below.

$$MB = 6.1866706334 - 0.2436578585 \times ST - 0.1417002387 \times WT - 0.1756984084 \times AT + 0.0008162107 \times SP - 0.0017057614 \times WP + 0.0009326694 \times AP \quad \text{(vii)}$$

where, ST, WT and AT are summer, winter and annual temperature respectively and SP, WP and AP are summer, winter and annual precipitation respectively. The coefficients are rounded up to 10 decimal places.

The trained regression model (Eq. vii) was then applied to estimate glacier mass balance from 1971 to 2100 across all SSP scenarios (Fig. 6b). The model results show relatively modest mass loss prior to 2000, followed by a gradual increase in mass loss rates, averaging around 0.5 m w.e. $a^{-1}$, which remained consistent across all SSP scenarios until approximately 2035. After 2035, the mass balance trajectories begin to diverge markedly, depending on the emission scenarios. Under the low-emission SSP126 scenario, the projected regional mass loss is expected to remain moderate, reaching a maximum of approximately 1.24 m w.e. $a^{-1}$ by the end of the century, with an average loss of 1.04 m w.e. $a^{-1}$ between 2035 and 2100. In contrast, under the high-emission SSP585 scenario, glacier mass loss is projected to intensify considerably, reaching up to 3.26 m w.e. $a^{-1}$ by 2100, with an average loss of 2.04 m w.e. $a^{-1}$ over the same period. Intermediate scenarios SSP245 and SSP370 indicate average mass losses of 1.38 m w.e. $a^{-1}$ and 1.69 m w.e. $a^{-1}$, respectively, during 2035–2100. These results underscore the increasing impact of future climatic changes on glacier health, with higher emissions leading to more pronounced mass loss.

#### 5.3.3. Mass balance sensitivity derived from CMIP6 and ERA5 Land reanalysis climate data

Simple linear regression between CMIP6 climate parameter and regional glacier mass balance revealed a strong negative correlation with all variables except winter precipitation, which showed a significant positive correlation (Fig. 7). Notably, all correlations were statistically significant (Fig. 7).

Temperature sensitivity analysis indicates the strongest response to summer temperature (−0.49 m w.e. $a^{-1}$ °$C^{-1}$) and the weakest to winter temperature (0.38 m w.e. $a^{-1}$ °$C^{-1}$). A 1 °C rise in annual temperature results in a mass loss of 0.42 m w.e. $a^{-1}$ °$C^{-1}$.

For precipitation, sensitivity is strongest for winter precipitation and lowest for summer precipitation (Table 3). Other than winter precipitation, an increase in all other climate parameters would lead to mass loss. A 10 % increase in summer and annual precipitation causes

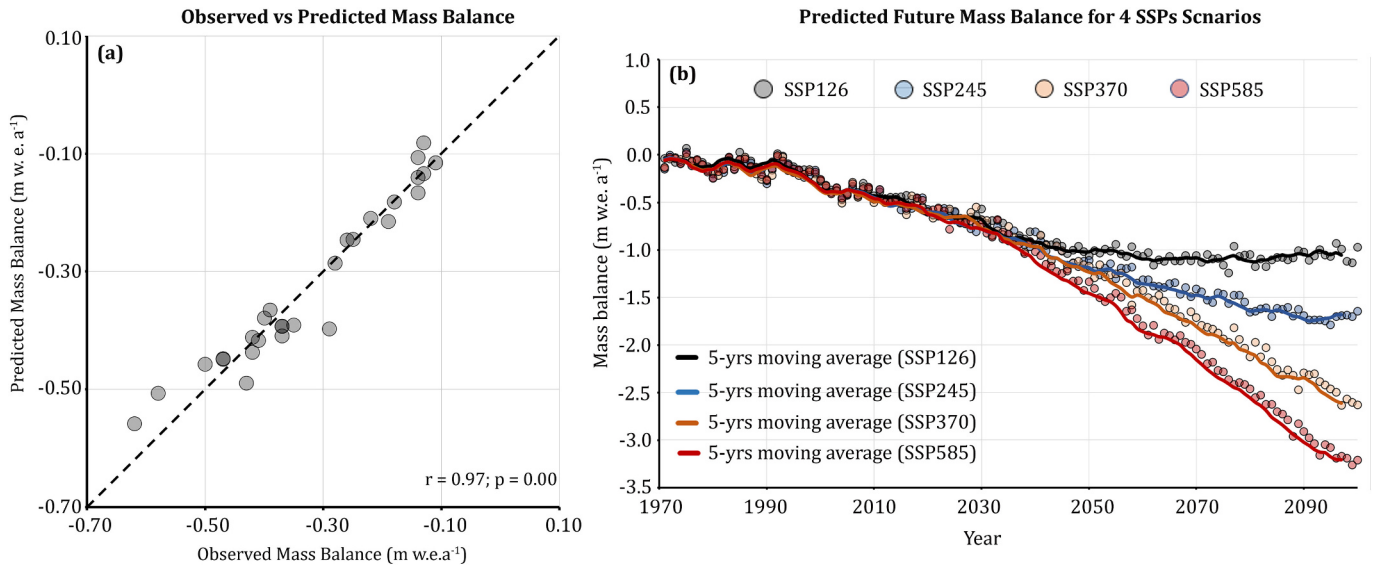


**Fig. 6.** (a) Observed vs. predicted mass balance using the Principal Component Regression model and (b) predicted future mass balance for all SSP's scenarios (For the simulation, average temperature and precipitation data from CMIP6 for four SSP scenarios—SSP126, SSP245, SSP370, and SSP585—were used, https://climexp.knmi.nl/).

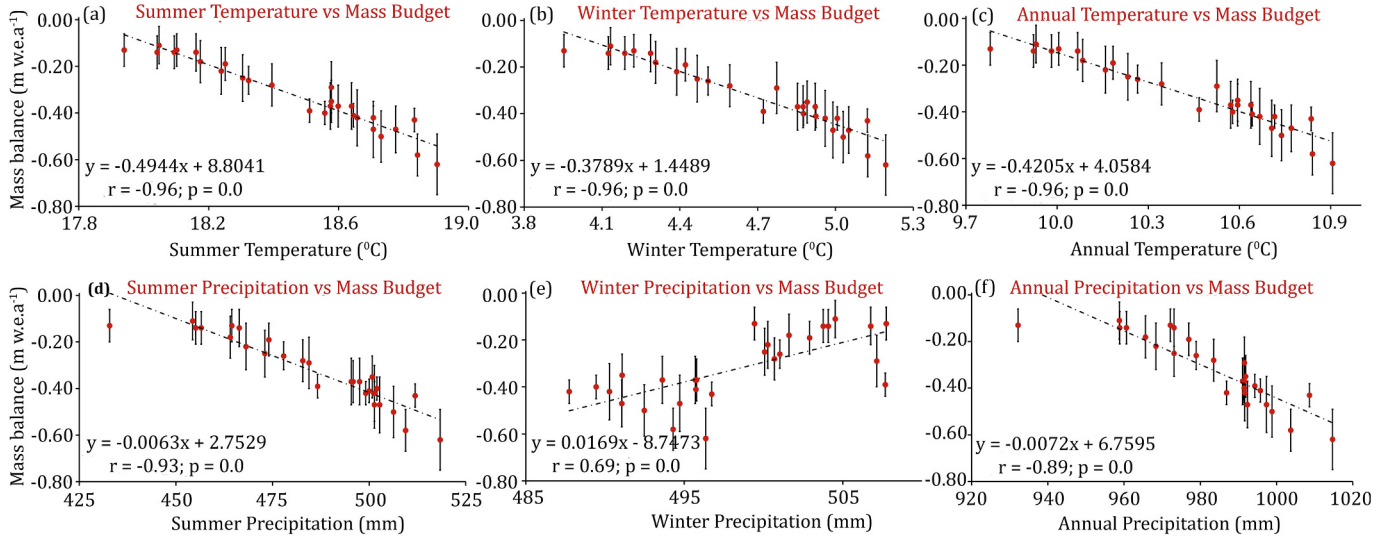


**Fig. 7.** Multi-temporal geodetic mass balance sensitivity with individual climate parameters based on average of 4 SSP's scenarios (a) summer temperature (b) winter temperature (c) annual temperature (d) summer precipitation (e) winter precipitation and (f) annual precipitation.

**Table 3**
Annual (A) and seasonal (summer: S, winter: W) mass balance sensitivity using CMIP6 and ERA5 Land reanalysis climate data.

| Using CMIP6 | | | |
|---|---|---|---|
| | $B_S$ | $B_W$ | $B_A$ |
| **$\beta_T$** | 0.49 | 0.38 | 0.42 |
| **$\beta_P$** | 0.31 | 0.84 | 0.71 |
| **Using ERA5 Land Reanalysis** | | | |
| **$\beta_T$** | 0.28 | 0.24 | 0.57 |
| **$\beta_P$** | 0.05 | 0.25 | 0.23 |

Unit of $\beta_T$: m w.e. $a^{-1}$ $°C^{-1}$; Unit of $\beta_P$: m w.e. $a^{-1}$ for 10 % increase in precipitation.

additional losses of 0.31 m w.e. $a^{-1}$ and 0.71 m w.e. $a^{-1}$, respectively, whereas a 10 % rise in winter precipitation offsets mass loss by 0.84 m w.e. $a^{-1}$.

Regression models for summer, winter, and annual temperatures yield geodetic glacier mass balance estimates of −0.24 to −0.25 m w.e. $a^{-1}$, closely matching the observed geodetic value of −0.25 ± 0.10 m w.e. $a^{-1}$. Similarly, precipitation-based models give values from −0.23 to −0.30 m w.e. $a^{-1}$, again consistent with observations for 1971–2022.

Future projections (2023−2100) suggest substantial increases in glacier mass loss, reaching 1.3 m w.e. $a^{-1}$ for summer temperature and 1.2 m w.e. $a^{-1}$ for winter and annual temperatures. Precipitation projections indicate mass losses of 0.8 m w.e. $a^{-1}$ for summer and annual precipitation, and 0.3 m w.e. $a^{-1}$ for winter precipitation.

Regression analysis using ERA5 Land reanalysis data shows some differences compared with CMIP6 results (Fig. 8). Summer and annual temperatures exhibited similar negative correlations with mass balance ($r = 0.41$–$0.42$), but with weaker statistical significance ($p = 0.03$–$0.02$). Winter temperature showed no significant relationship ($p = 0.4$). Summer precipitation also displayed a weak, non-significant relationship ($r = 0.17$; $p = 0.4$). In contrast, both annual and winter precipitation

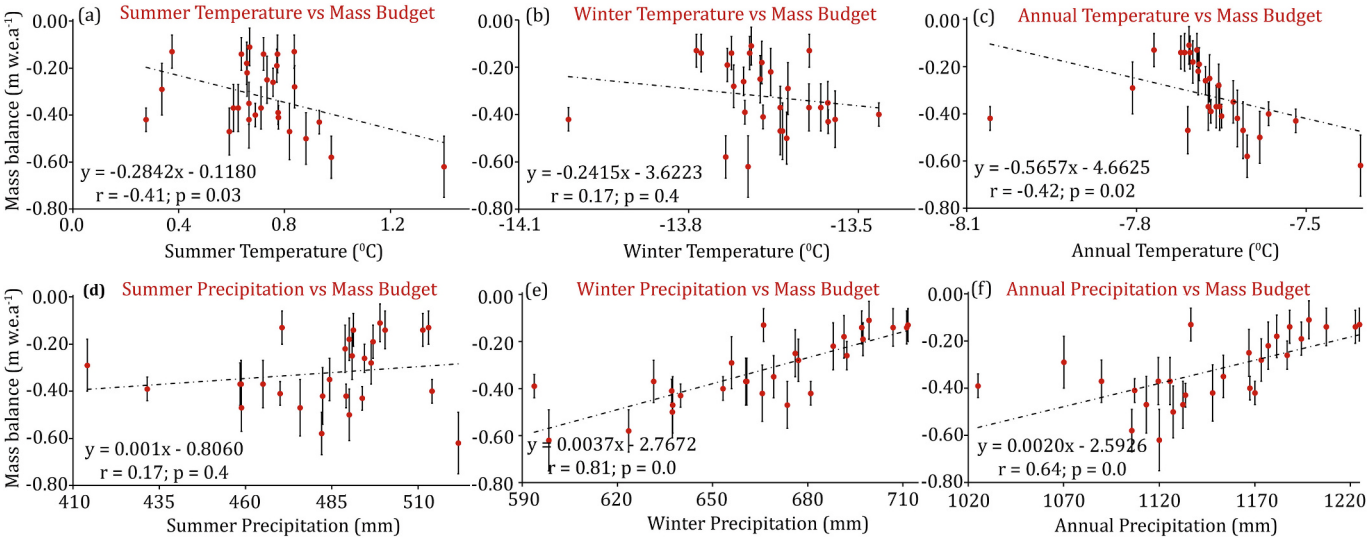


**Fig. 8.** Multi-temporal geodetic mass balance sensitivity with individual climate parameters based on ERA5 Land reanalysis climate data (a) summer temperature (b) winter temperature (c) annual temperature (d) summer precipitation (e) winter precipitation and (f) annual precipitation.

demonstrated strong, statistically significant positive correlations with mass balance ($r = 0.64$–$0.81$; $p = 0.0$), underscoring their predominant role under current climatic conditions.

Mass balance sensitivities from ERA5 Land reanalysis data (Table 3) indicate that annual temperature has a stronger influence than seasonal temperature; a 1 °C rise in annual temperature results in a mass balance of −0.57 m w.e. $a^{-1}$ $°C^{-1}$, compared to −0.28 m w.e. $a^{-1}$ $°C^{-1}$ for summer temperature. These sensitivities are lower than those derived from CMIP data.

Precipitation sensitivity indicates that glaciers in the region gain mass from winter ($\beta_P = 0.25$ m w.e. $a^{-1}$) and annual precipitation ($\beta_P = 0.23$ m w.e. $a^{-1}$). However, these sensitivities are less pronounced compared to CMIP6 sensitivities.

We have observed discrepancies between CMIP6 and ERA5 Land reanalysis results which can be attributed to several factors. The ERA5 Land reanalysis data is relatively high spatial resolution (0.1°–0.25°), which captures fine-scale climatic variability that is particularly relevant in the complex topographic setting of the Himalaya. In contrast, CMIP6 global climate models operate at coarser resolutions (1°–2.5°), which tend to smooth localized signals, especially those related to orographic precipitation and valley-scale temperature gradients (Dimri et al., 2013). Additionally, ERA5 Land reanalysis assimilates multiple observational datasets and is therefore better constrained by present-day variability, whereas CMIP6 outputs are purely model-driven projections that can exhibit systematic biases in both temperature and precipitation across the Himalaya (Zhu and Yang, 2020). Finally, ERA5 Land reanalysis represents reanalysis of past climate conditions, while CMIP6 integrates both historical and future scenarios under prescribed radiative forcing, making their sensitivities not strictly comparable (Eyring et al., 2016).

Overall, these differences emphasize the complementary strengths of the two datasets, whereby ERA5 Land reanalysis provides greater observational fidelity in representing present-day glacier–climate interactions, while CMIP6 offers valuable insights into long-term climate forcing and future trajectories, albeit with increased uncertainties at the basin scale. At the same time, the above differences between CMIP6- and ERA5 Land reanalysis-based sensitivities raise important questions about which dataset better represents the region's climate, particularly in relation to temperature–mass balance relationships and the role of winter precipitation.

## 6. Discussions

### 6.1. Comparison of glacier area and length changes with previous studies

Regional and glacier-specific variations in glacier area and length changes covering our study area have been widely studied (Kulkarni et al., 2011; Pandey and Venkataraman, 2013; Garg et al., 2017; Mukherjee et al., 2018; Sahu and Gupta, 2020; Patel et al., 2021). However, direct quantitative comparisons with our results remain difficult due to differences in data sources, glacier populations, time scales, and inventory baselines. Unlike many prior studies that analyzed a single time interval, our assessment covers multiple periods and includes both debris-covered and clean-ice glaciers. Overall, our results align with the regional trend of glacier retreat, though we observed notable temporal variability (Table 4).

We estimated a slightly higher glacier area loss (~3.7 %; 0.08 % $a^{-1}$ during 1971–2017) than Mukherjee et al. (2018), who reported ~1.7 % (0.04 % $a^{-1}$) during a nearly similar timeframe (1971–2015). This difference may be due to higher spatial coverage (17 % more glacierized area) and a higher minimum glacier size (>2 $km^2$) in their study. In contrast, our reduction rates are lower than those reported by Kulkarni et al. (2011); 0.52 % $a^{-1}$) and Patel et al. (2021); 0.21 % $a^{-1}$), possibly due to the use of lower-accuracy Survey of India maps and differing glacier selection criteria. Despite such variations, our results compare well with other studies. Sahu and Gupta (2020) observed a loss rate of 0.11 ± 0.04 % $a^{-1}$ (1971–2016), while Pandey and Venkataraman (2013) reported ~0.08 % $a^{-1}$ between 1980 and 2010. More recently, Vatsal et al. (2024) quantified glacier area reduction in the Chandra Basin at 0.09 ± 0.03 % $a^{-1}$ over the period 1993–2019 (Table 4).

Individual glaciers showed variable changes. For Chhota Shigri Glacier, our estimate (1971–2022) shows an area loss of 0.04 % $a^{-1}$ and frontal retreat of 5.7 ± 1.01 m $a^{-1}$, in line with previous studies. For example, Mukherjee et al. (2018) and Sahu and Gupta (2020) reported area loss rates of 0.03 % and 0.02 % $a^{-1}$, respectively, with similar retreat rates. Garg et al. (2017) and Pandey and Venkataraman (2013) also reported comparable trends. Similar variability was observed for Bara Shigri and Samudra Tapu glaciers (Table 4).

### 6.2. Regional and individual geodetic glacier mass balance variability

The overall glacier mass balance estimated in this study is consistent with global geodetic assessments (Brun et al., 2017; Hugonnet et al.,

**Table 4**
Comparison of area/retreats of regional & some individual glaciers with previous studies.

| SL No. | Glacier Area ($km^2$) | No of glaciers (N) | Time period | Data used | Area Change (% $a^1$) | Reference | This study (N = 348; Area in 1971: 798.9 ± 54.2 $km^2$) | |
|---|---|---|---|---|---|---|---|---|
| | | | | | | | Time Span | Area Change (% $a^1$) |
| **Regional Glacier** | | | | | | | | |
| 1 | 960 ± 20 | 198 | 1971–2015 | KH 4B Corona; ASTER; Cartosat-1 | −0.04 | Mukherjee et al. (2018) | 1971–2017 | −0.08 |
| 2 | 696 | 116 | 1962–2001 | SOI-Toposheet; IRS LISS-III | −0.52 | Kulkarni et al. (2011) | 1971–2012 | −0.06 |
| 3 | 1306 ± 65 | 257 | 1971–2018 | KH 4B Corona; Sentinel 2 | −0.21 | Patel et al. 2021 | 1971–2017 | −0.08 |
| 4 | 639.4 ± 5.8 | 156 | 1971–2016 | KH 4B Corona; Sentinel 2 | −0.11 | Sahu and Gupta (2020) | 1971–2017 | −0.08 |
| 5 | 377.6 | 15 | 1980–2010 | Landsat MSS, TM; LISS; AWiFS | −0.08 | Pandey and Venkataraman (2013) | 1981–2012 | −0.05 |
| 6 | 696 ± 62 | 251 | 1993–2019 | Landsat TM ETM+ & OLI | −0.09 | Vatsal et al. (2024) | 1971–2022 | −0.09 |
| **Individual Glacier** | | | | | | | | |
| **Glacier Name** | | **Time Span** | **Length change (m $a^{-1}$)** | **Area Change (% $a^1$)** | | **Reference** | | |
| Chhota Shigri RGI60–14.15990 | | 1971–2015 | −5.9 ± 0.44 | −0.03 | | Mukherjee et al. (2018) | | |
| | | 1971–2016 | −5.8 ± 0.50 | −0.02 | | Sahu and Gupta (2020) | | |
| | | 1993–2014 | −4.1 ± 2.52 | −0.06 | | Garg et al. (2017) | | |
| | | 1980–2010 | −7.7 | −0.02 | | Pandey and Venkataraman (2013) | | |
| | | 1971–2022 | −5.7 ± 1.01 | −0.04 | | This study | | |
| Bara Shigri RGI60–14.15447 | | 1971–2015 | −27 ± 0.44 | −0.02 | | Mukherjee et al. (2018) | | |
| | | 1971–2016 | −27.6 ± 0.50 | −0.02 | | Sahu and Gupta (2020) | | |
| | | 1980–2010 | −18.67 | −0.05 | | Pandey and Venkataraman (2013) | | |
| | | 1993–2014 | −15.5 ± 2.52 | −0.04 | | Garg et al. (2017) | | |
| | | 1971–2022 | −28.4 ± 1.01 | −0.02 | | This study | | |
| Samudra Tapu RGI60–14.15613 | | 1971–2015 | −21 ± 0.44 | −0.02 | | Mukherjee et al. (2018) | | |
| | | 1971–2016 | −23.5 ± 0.50 | −0.04 | | Sahu and Gupta (2020) | | |
| | | 1980–2010 | −19.90 | −0.08 | | Pandey and Venkataraman (2013) | | |
| | | 1962–2000 | −19.5 | −0.29 | | Kulkarni et al. (2006) | | |
| | | 1971–2022 | −23.4 ± 1.01 | −0.05 | | This study | | |

2021), (Supplementary Fig. S1). Our mass loss rate of 0.47 ± 0.12 m w. e. $a^{-1}$ for 2002–2022 is slightly higher, yet remains within the uncertainty ranges from the data by Brun et al. (2017) (0.37 ± 0.09 m w.e. $a^{-1}$ for 2000–2016) and Hugonnet et al. (2021) (0.41 ± 0.05 m w.e. $a^{-1}$ for 2000–2020). For a more detailed comparison of our results with previously published studies, including time periods, methodologies and associated uncertainties, we refer to Supplementary Table T6.

While our estimates align with global trends of glacier mass loss, regional comparisons show notable variability. Consistent with previous findings, we find limited pre-2000 (0.11 ± 0.08 m w.e. $a^{-1}$ for 1971–2002) and accelerated post-2000 (0.37 ± 0.10 m w.e. $a^{-1}$ for 2002–2017) mass loss (Fig. 9a). These results closely match Mukherjee et al. (2018), who reported mass balance of −0.07 ± 0.1 m w.e. $a^{-1}$ (1971–1999) and − 0.36 ± 0.1 m w.e. $a^{-1}$ (1999–2013). Maurer et al. (2019) also found comparable values (−0.14 ± 0.10 m w.e. $a^{-1}$ for 1975–2000) in Lahaul-Spiti using Hexagon and ASTER data (Fig. 9a).

Vincent et al. (2013) and Gardelle et al. (2013) reported mass balances of −0.44 ± 0.09 and − 0.45 ± 0.13 m w.e. $a^{-1}$ (1999–2011), slightly more negative than our −0.37 ± 0.10 m w.e. $a^{-1}$ (2002−2012). Kääb et al. (2012) found a less negative value (−0.30 ± 0.04 m w.e. $a^{-1}$ for 2003–2008), possibly due to broader regional coverage. Vijay and Braun (2016) reported a higher loss of 0.65 ± 0.43 m w.e. $a^{-1}$ (2000−2012), likely due to differing uncertainty methods. Ramsankaran et al. (2019) estimated mass balance of −0.68 ± 0.15 m w.e. $a^{-1}$ (1999–2013) for Chandra basin, more negative than our −0.47 ± 0.12 m w.e. $a^{-1}$ (2002−2022), possibly due to glacier selection and lack of radar penetration correction.

Multiple studies have assessed individual glaciers (Fig. 9b–c, Supplementary Table T6), especially Chhota Shigri Glacier, which is the only Indian reference glacier having more than twenty years of glaciological mass balance records. Satellite-based estimates post-2000 range from −0.15 to −0.77 m w.e. $a^{-1}$, mostly aligning with our −0.57 ± 0.16 m w.e. $a^{-1}$ (2002–2022), except Garg et al. (2017), who reported −0.77 ± 0.22 m w.e. $a^{-1}$.

Despite broad agreement, temporal differences persist. Our 2005–2012 estimate (−0.32 ± 0.13 m w.e. $a^{-1}$) aligns with Mukherjee et al. (2018) (−0.24 ± 0.10 m w.e. $a^{-1}$), but our 1971–2012 value (−0.31 ± 0.12 m w.e. $a^{-1}$) is more negative than theirs (−0.08 ± 0.10 m w.e. $a^{-1}$). Similarly, our post-2000 estimate (−0.56 ± 0.16 m w.e. $a^{-1}$) is more negative than Brun et al. (2017) (−0.31 ± 0.09 m w.e. $a^{-1}$) and Hugonnet et al. (2021) (−0.22 ± 0.05 m w.e. $a^{-1}$), but comparable to Azam et al. (2024) (−0.43 ± 0.08 m w.e. $a^{-1}$). This difference may result from our use of modified polygons which isolated Chhota Shigri Glacier from its neighbouring glacier, while the others used unmodified RGI 6.0 outlines.

Our mass balance estimate for Bara Shigri Glacier (−0.46 ± 0.16 m w.e. $a^{-1}$ for 2002–2022) aligns well with Brun et al. (2017) and Hugonnet et al. (2021) data, which shows −0.41 ± 0.09 m w.e. $a^{-1}$ for 2000–2016/2020. The pre-2000 estimate (−0.15 ± 0.11 m w.e. $a^{-1}$ for 1971–2002) is also consistent with Mukherjee et al. (2018). Hamtah Glacier shows similar post-2000 losses, with a notable increase to 0.75 ± 0.18 m w.e. $a^{-1}$ after 2014. However, the mass loss might be slightly overestimated as this glacier had a strong ice avalanche contribution which is difficult to asses using the geodetic method (Laha et al., 2017).

While long-term glacier mass loss estimates from various datasets, time periods, and methodologies remain broadly consistent within uncertainty limits, our multi-temporal geodetic mass balance analysis offers a distinct advantage by capturing the temporal variability in glacier mass loss. This approach reveals that mass loss rates are not uniform over time or across individual glaciers, underscoring the importance of temporal resolution in glacier monitoring. By resolving these intertemporal variations, our study enhances understanding of glacier dynamics and their sensitivity to regional climate variability, providing valuable insights for both scientific assessments and climate adaptation strategies.

### *6.3. Comparison of SSPs and ERA5 Land reanalysis climate data with weather station data*

An overall increase in summer, winter, and annual temperatures was

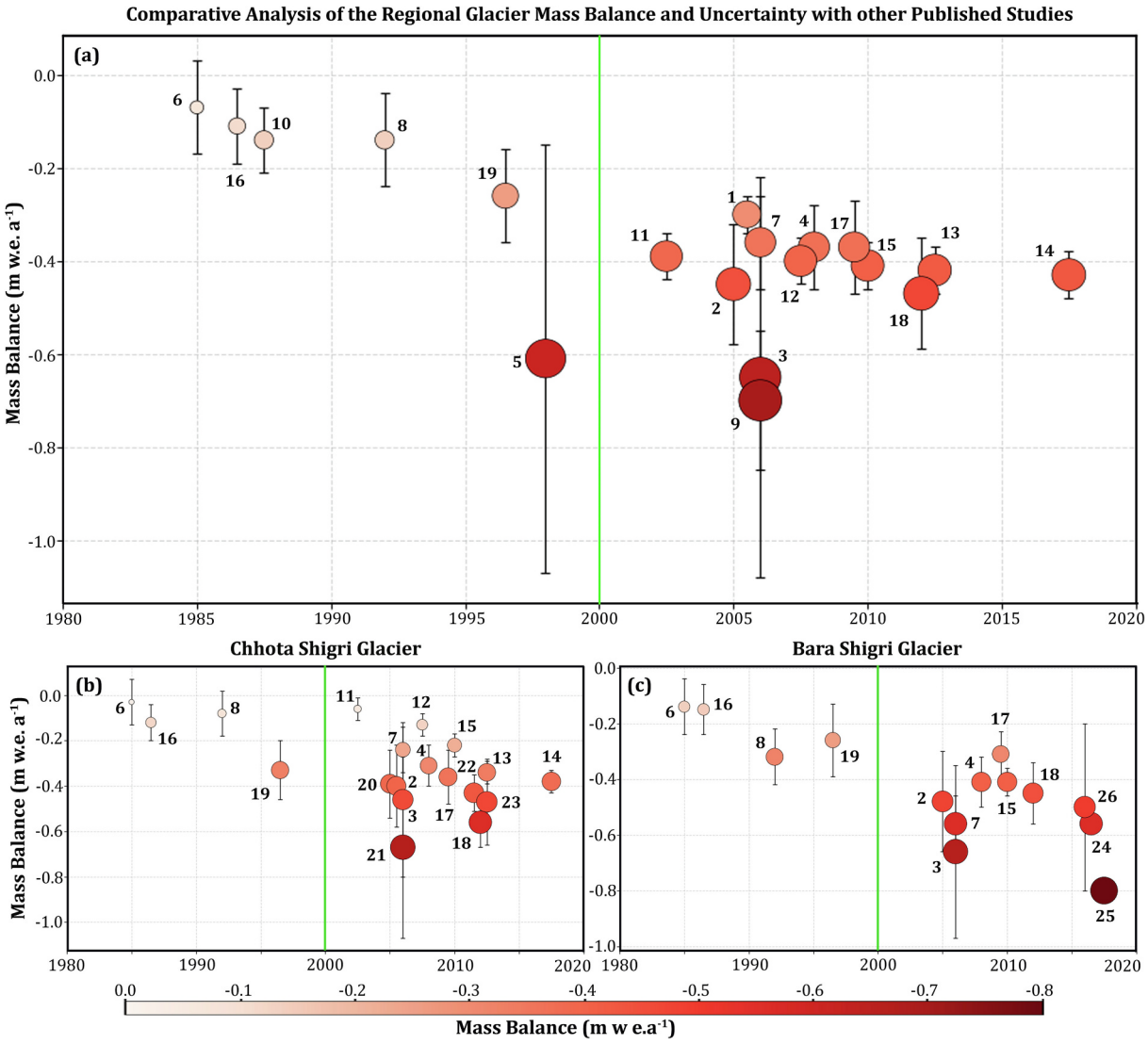


**Fig. 9.** The mass budget as estimated by various authors in Lahul-Spiti region (a) Regional glaciers, (b) Chhota Shigri and (c) Bara Shigri. The size of the scatter points and the colour represent the mass balance value. The error bar represents the uncertainty associated with the mass budget (1: Kääb et al. (2012); 2: Gardelle et al. (2013); 3: Vijay and Braun (2016); 4: Brun et al. (2017); 5: Tawde et al. (2017); 6–8: Mukherjee et al. (2018); 9: Ramsankaran et al. (2019); 10: Maurer et al. (2019); 11–15: Hugonnet et al. (2021); 16–19: This study; 20: Vincent et al. (2013); 21: Azam et al. (2012); 22–23: Azam et al. (2024); 24–25: WGMS (2024) and 26: Patel et al. (2021)).

observed during 1971–2022, whereas seasonal (summer and winter) precipitation displayed divergent patterns throughout the observation period based on the average of all CMIP6 SSP scenarios. In 2022, the summer temperature peaked at approximately 19.0 °C, which was 0.7 °C above the long-term average of 18.3 °C. *Prior* to 2000, the average summer temperature was around 18.0 °C, rising to about 18.7 °C for the period 2000-2022. Similarly, winter and annual temperatures increased by 0.9 °C and 0.8 °C, respectively, when compared with the post-2000 period to the pre-2000 period. All three temperature measures—summer, winter, and annual—exhibited a strong positive correlation with time (ranging from 0.93 to 0.95, $p = 0.00$). In contrast, the average SSP outputs for precipitation revealed seasonally divergent trends: summer precipitation increased by ~11 % after 2000 with a significant positive correlation with time ($r = 0.83$, p = 0.0), whereas winter precipitation declined slightly (~1.4 %) after 2000 but showed an insignificant correlation ($r = 0.12$, $p = 0.4$). Annual precipitation, consistent with the summer trend, increased by approximately 5 % post-2000 with a significant positive correlation ($r = 0.73$, $p = 0.0$).

ERA5 Land reanalysis data also indicated a similar warming trend in temperatures as observed in the average SSPs, though the precipitation patterns differed. The average summer temperature increased by approximately 0.3 °C after 2000 compared to the pre-2000 period, whereas winter and annual temperatures also rose (by 0.04 °C and 0.14 °C, respectively), though these increases were not statistically significant. In contrast to the average SSP data, ERA5 Land reanalysis winter and annual temperatures did not show significant correlations with time ($r = 0.02$, $p = 0.9$ and $r = 0.18$, $p = 0.2$, respectively), while summer temperature exhibited a significant, albeit weaker than average SSPs, correlation with time ($r = 0.24$, $p = 0.04$). On the other hand, ERA5 Land reanalysis precipitation trends diverged from SSPs: both summer and annual precipitation decreased by approximately 5.6 % and 10.2 %, respectively, after 2000, while winter precipitation showed a marked decline of about 13 % relative to pre-2000 levels, consistent with the SSP-based estimates.

Meteorological observations from the Bhuntar station reflected broadly similar patterns. During 2000–2022, summer, winter, and annual temperatures increased by approximately 0.7 °C, 0.8 °C, and 0.6 °C, respectively, relative to 1971–2000. Precipitation showed contrasting seasonal changes: winter precipitation decreased by ~14 % after 2000 compared to the pre-2000 period, whereas summer

precipitation increased by ~11 % over the same interval. Both summer and annual temperatures exhibited significant positive correlations with time ($r = 0.41$, $p = 0.0$ and $r = 0.47$, p = 0.0, respectively), while the winter temperature trend was not statistically significant ($r = 0.21$, $p = 0.15$). In contrast, none of the precipitation components demonstrated a significant correlation with time.

Although the average SSPs, ERA5 Land reanalysis and Bhuntar station records revealed heterogeneous trends, direct comparisons were constrained by elevation differences and the influence of **e**levation-dependent climate variability. To refine the comparison, SSP and ERA5 Land reanalysis grid cell data corresponding to the Bhuntar station location were used (Supplementary Fig. S2). This analysis yielded significant correlations between average SSPs with station data for temperatures, summer (r = 0.47, $p = 0.00$), winter ($r = 0.29$, $p = 0.05$), and annual ($r = 0.56$, p = 0.00) respectively. Whereas, the ERA5 Land reanalysis temperature data showed similar trend but comparatively stronger correlation with the station data for summer ($r = 0.59$, p = 0.0), winter ($r = 0.39$, p = 0.0) and annual ($r = 0.57$, p = 0.0). Similarly, summer ($r = 0.36$, $p = 0.01$) and winter ($r = 0.33$, $p = 0.02$) precipitation of SSPs also showed significant correlation, however, annual ($r = 0.16$, $p = 0.51$) precipitation indicated weak or no statistical relationship. The ERA5 Land reanalysis precipitation correlation with station data (summer: r = 0.41, p = 0.0; winter: $r = 0.79$, p = 0.0 and annual: r = 0.41, p = 0.0) also exhibited similar but strong correlation as compared to average SSPs.

The lack of correlation in annual precipitation between SSP model outputs and station observations is mainly attributed to the mismatch in spatial scale. Where climate models represent area-averaged values over large grid cells (typically 100–250 km), stations provide point-based measurements. Additionally, model biases in capturing local precipitation dynamics, especially in **t**opographically complex regions, contribute to this disparity (Sun et al., 2018). These differences are further amplified by the limited temporal and spatial resolution of climate models, which restricts their ability to simulate short-term, localized rainfall events effectively (Sun et al., 2018).

Moreover, ERA5 Land reanalysis shows slightly higher correlation than average SSPs with station precipitation because it assimilates in-situ observations and better captures regional variability, whereas CMIP6 SSPs operate at coarser scales and are not directly constrained by observations (Eyring et al., 2016). This explains the weaker correspondence of SSP precipitation with station data compared to ERA5 Land reanalysis data.

### 6.4. Temporal and seasonal climate variability

To understand the seasonal variation of the climate parameters and their influence on regional geodetic glacier mass balance, we defined four seasons, namely, summer (June-Sept), autumn (Oct-Nov), winter (Dec-March) and spring (Apr-may) in our analysis (Fig. 10). In general, temperature has consistently increased in all seasons, while precipitation shows an increasing trend only in summer. Average winter precipitation remained relatively stable, showing only a slight decrease of approximately 1.5 % in the post-2000 period compared to the pre-2000 period. Mukherjee et al. (2018), using NCEP, PREC/L, and ERA-Interim data, reported an increase in winter precipitation after 2000, while APHRODITE data showed a significant decrease. Summer temperatures increased (0.7 °C) from 2000 to 2022 compared to 1971–2000. Azam et al. (2014) also found a rise in summer temperatures and decrease in winter precipitation from 2001 to 2012 relative to 1986–2000, based on data from a station near the Chhota Shigri glacier.

Mean autumn temperatures increased (~0.8 °C) after 2002 and reached ~1.0 °C in 2017–2022. We also observed a persistent positive anomaly of summer-autumn transition (Sept-Oct) temperature throughout the observation period with a temperature increase of ~0.7 °C during last glacier mass balance period (2017–2022) compared to the average summer-autumn transition temperature. Since 2000, temperatures during the spring–summer transition (May–June) increased by approximately 0.7 °C compared to the pre-2000 period, with a further increase of about 0.9 °C observed during 2017–2022. Additionally, post-2000, autumn precipitation decreased insignificantly (1 %) compared to pre-2000, while spring precipitation increased by ~3 %. Our findings suggest that though the precipitation does not significantly affect the melting rate, rising temperatures during the summer–autumn and spring–summer transitions may prolong the ablation

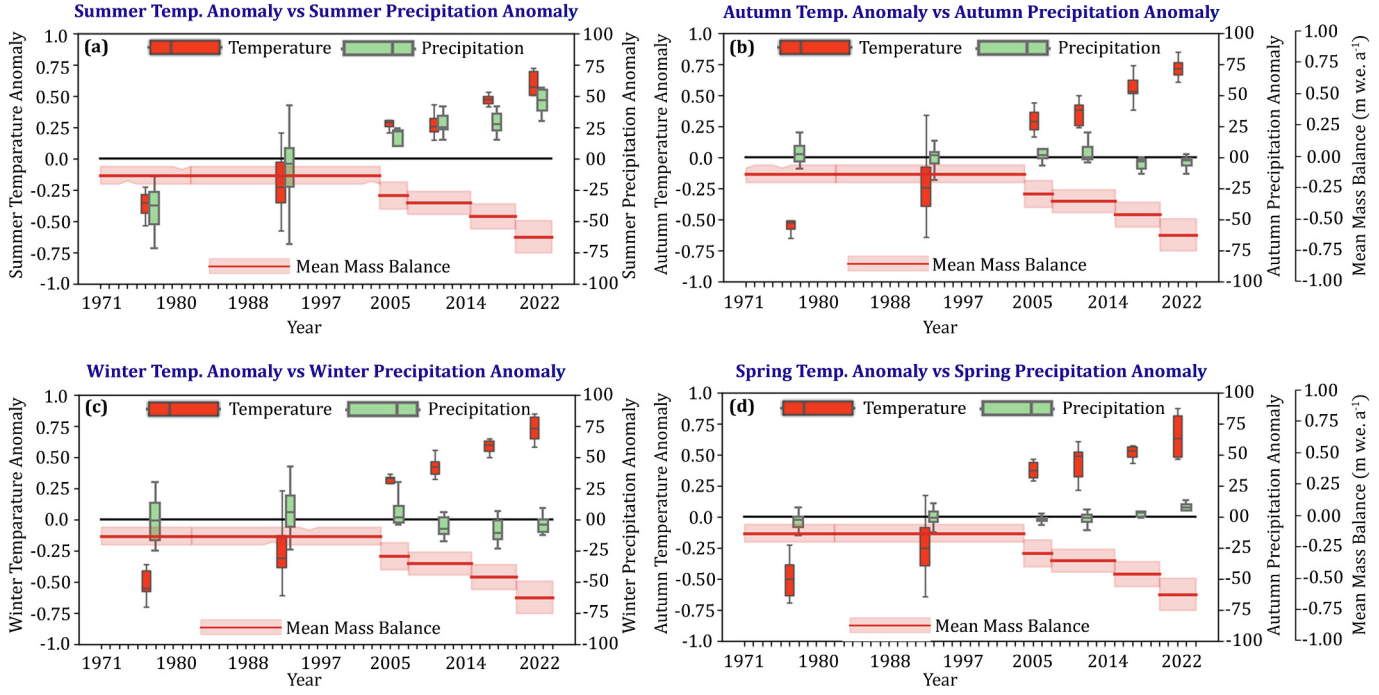


**Fig. 10.** Seasonal variations of climate driver's anomaly (a) summer temperature and annual precipitation (b) autumn temperature and precipitation (c) winter temperature and precipitation and (d) spring temperature and precipitation with multi-temporal glacier mass balance.

season and hence increase melt.

### 6.5. Influence of individual climate drivers on regional glacier mass balance variability

Future precipitation projections (2023–2100) under different SSP scenarios indicate a 12 % to 27 % (with an average of approximately 19 %) increase in summer precipitation after 2022, whereas winter precipitation remain nearly unchanged or shows only a negligible increase (approximately 1 %) over the same period. Both increase in summer precipitation, and considerable glacier mass loss is projected—likely because, in monsoon-influenced or transitional climate zones, enhanced summer precipitation often coincides with warmer temperatures. This leads to intensified melting, as a substantial portion of the precipitation falls as rain rather than snow, especially at mid-to-low elevations, thereby contributing directly to surface melt through latent heat release and reduced surface albedo (Sakai and Fujita, 2017). Azam et al. (2024) also reported that in transitional regions influenced by both monsoon and westerlies, increased summer precipitation, if occurring as rainfall or during peak melt periods, may exacerbate glacier mass loss. Slight increase in winter precipitation can also enhance melting probably due to warmer winter temperatures (increased 1.5 °C after 2022), shifts from snow to rain mainly at the beginning and the end of the winter months, and energy balance feedbacks. This phenomenon was also observed in other parts of HMA region particularly in climate transition zone in the western Himalaya and Karakoram (Azam et al., 2024).

Our estimated regional glacier mass balance sensitivity to summer temperature ($-0.49$ m w.e. $a^{-1}$ °$C^{-1}$) closely aligns with that of the Chhota Shigri Glacier reported elsewhere ($-0.52$ m w.e. $a^{-1}$ °$C^{-1}$, Azam et al., 2014 and $-$ 0.43 m w.e. $a^{-1}$ °$C^{-1}$, Mukherjee et al., 2025) are presented using different modelling approaches. This alignment supports the robustness of the multi-temporal geodetic mass balance modelling approach used in this study, highlighting its potential for application across other Himalayan regions to investigate glacier–climate interactions and project future mass balance changes. Given that summer temperature exerts the strongest control on glacier mass balance reconstructing regional mass balance time series using temperature records appears to be a feasible and effective strategy.

The regional sensitivity to winter precipitation based on average SSPs (+0.84 m w.e. for 10 % increase) is significantly higher than the Chhota Shigri glacier's estimated precipitation sensitivity reported elsewhere (+0.16 m w.e. $a^{-1}$ per 10 % increase in precipitation, Azam et al., 2014; +0.27 m w.e. $a^{-1}$ for 30 % change in precipitation, Mukherjee et al., 2025). This likely arises from the spatial averaging of CMIP6 precipitation over a much larger area when calculating the regional sensitivity compared to the point based meteorological station data used by Azam et al. (2014) and 10 km resolution ERA5 Land reanalysis data used by Mukherjee et al. (2025). Additionally, precipitation exhibits greater spatial variability and uncertainty over mountainous regions than temperature (Rasmussen et al., 2012; Silverman and Maneta, 2016), further contributing to discrepancy. It is worth noting that the region is projected to experience continuous glacier mass loss throughout the century—despite increases in summer and annual precipitation. A 10 % rise in these variables is associated with further mass loss, while only an increase in winter precipitation has the potential to offset the negative mass balance. Projections under the optimistic scenario (SSP126) suggest that by 2100, summer and annual precipitation may increase by approximately 19 % and 6 %, respectively, while winter precipitation, the principal source of glacier accumulation, will remain almost unchanged, with only a negligible rise of about 1 %. Under the high-emission scenario (SSP585), summer and annual precipitation are projected to increase by around 27 % and 13 %, respectively, whereas winter precipitation may decline by approximately 1 %. These findings indicate that, regardless of the emission pathway, limited enhancement or reduction of winter precipitation is likely to constrain glacier accumulation. Consequently, sustained glacier mass loss in the region appears probable even under optimistic climate trajectories, with potentially amplified losses under high-emission conditions.

ERA5 Land reanalysis data indicate that annual temperature sensitivity ($-0.57$ m w.e. $a^{-1}$) exceeds that of seasonal temperatures (Table 3). Although ERA5 Land reanalysis also shows that glaciers in the region accumulate mass from winter and annual precipitation, the values are not as high as indicated by CMIP6 projections (Table 3). The differences in sensitivity values can be attributed to differences in spatial resolution, climate variability representation, bias correction, as well as modelling assumptions (Wang et al., 2021).

Additionally, ERA5 Land reanalysis data suggests that a 25 % increase in both annual and winter precipitation would be required to offset the mass loss associated with a 1 °C rise in annual temperature. This estimate aligns well with previous studies, which indicated that approximately a 30 % increase in precipitation is necessary to counterbalance a + 1 °C warming at the Chhota Shigri Glacier (Sahu et al., 2024). Long-term trends (1971–2022) from ERA5 Land reanalysis data reveal that despite an increase in all temperature components since 2000, winter and annual precipitation have declined by 12 % and 10 %, respectively. If this trend continues in the near future, precipitation changes will likely be insufficient to offset the warming-induced mass loss, leading to substantial glacier retreat in the region.

### 6.6. Implications for wider Himalaya

Projected changes in temperature and precipitation under different SSP scenarios will substantially impact the future glacier mass balance. Notably, nearly unchanged winter precipitation, along with increased summer and annual precipitation, will further intensify glacier mass loss through the end of the 21st century. In extended projections for the period 2075–2100, we observed that though the glacier mass loss may stabilize under SSP126 (< 1 % increase), a substantial mass loss of 23–54 % is likely under intermediate to high-emission scenarios. These findings emphasize the urgent need for sustained and aggressive climate action, even under optimistic emission pathways, to curb future glacier loss (Matthews et al., 2021).

The average ice thickness in this region in 2022 (using thickness maps from Farinotti et al. (2019) and considering elevation change $-11.01 \pm 2.82$ m during 2002–2022 from our analysis) was approximately 110 m. Our analysis indicates that the average rate of ice thickness loss will be 1.0 m $a^{-1}$ during the period 2023–2100. Consequently, even under the optimistic emission scenario (SSP126), ongoing climate change may lead to a regional glacier volume loss of approximately 69 % by the end of the 21st century, assuming a constant glacier area. Miles et al. (2021) estimated that, even without accounting for further warming, the total glacier ice volume across High Mountain Asia (HMA) could decrease by 21 % ± 1 % by century's end due to the existing climatic-geometric imbalance. In their regional assessment, they projected about 38 % ice volume loss for Lahaul-Spiti under similar conditions. Our estimate exceeds their findings, likely due to differences in the glacierized area considered. Miles et al. (2021) included 3381 $km^2$ of glacier area, and did not factor in future warming. Additionally, under similar climate change conditions and even in the SSP126 scenario, we found that most small glaciers (average thickness: 23.5 ± 11.2 m in 2000; Farinotti et al., 2019) are projected to lose ice at an average rate of approximately 0.7 m $a^{-1}$ during 2000–2050 and may disappear before the middle of this century.

As glacier retreat progresses, the replacement of high-albedo glacier ice and snow surfaces by lower-albedo debris or exposed bedrock enhances local energy absorption, thereby intensifying melt rates and accelerating negative mass balance trends. This albedo–melt feedback has been widely recognized as a key amplifying process in glacier–climate interactions (Brock et al., 2010). The effect is particularly critical for small glaciers with limited ice reserves, as their reduced resilience makes them more susceptible to rapid volume loss once feedback

processes become dominant (Huss and Hock, 2018). Consequently, the persistence of small glaciers under projected warming scenarios is further threatened by this feedback, increasing the likelihood of their disappearance by mid-century.

However, climate models have inherent limitations, and associated uncertainties tend to increase with projections for longer lead times (Collins et al., 2012). Therefore, the projected impacts of climate on glacier mass balance must be interpreted within this context. These impacts may evolve as new climate scenarios become available or as we approach the projected timeframes, potentially reducing uncertainty.

Using a basic positive degree day mass balance model, Rasmussen (2013) found that temperature sensitivity of mass balance for eight High Mountain Asia (HMA) glaciers monitored by the World Glacier Monitoring Service (WGMS) varied between −0.5 and − 0.2 m w.e. $a^{-1}$ °$C^{-1}$. In a similar context, the Tuyuksu Glacier, located in the Northern Tien Shan in Kazakhstan, demonstrated a sensitivity value of −0.4 m w.e. $a^{-1}$ °$C^{-1}$. Wang et al. (2019) examined 45 HMA glaciers with in-situ mass balance data available for a minimum of two years, and reported an average mass balance sensitivity in the range of −0.59 to −0.4 m w.e. $a^{-1}$ °$C^{-1}$. Engelhardt et al. (2015), using a simplified melt index approach, assessed four glaciers in Norway and found their annual mass balance sensitivity to temperature to fall between 0.55 and 1.74 m w.e. $a^{-1}$ $K^{-1}$. However, mass balance sensitivity to precipitation for this region does not coincide with the findings by Wang et al. (2019) and Engelhardt et al. (2015), who estimated 0.22 m w.e. $a^{-1}$ and 0.5–1.39 m w.e. $a^{-1}$ for 30 % increase in precipitation.

Winter precipitation showed a slight decline in 2000–2022 compared to the pre-2000 period, while winter temperature increased. Regional glacier mass loss was also positively correlated with winter temperature. Therefore, probably the overall accumulation likely remains limited, and temperature-driven melt processes dominate glacier mass balance. As a result, small variations in precipitation have only a minor influence on net mass balance, while temperature fluctuations exert a much more direct and amplified impact (Sakai and Fujita, 2017).

The mass balance response in this study is derived solely from CMIP6 climate data. The differences observed in mass balance sensitivity estimates when using ERA5-Land reanalysis climate data raise concerns about the reliability of various climate datasets. These datasets are derived from different climate models, which are calibrated and validated using observations from meteorological stations. In data-scarce regions such as the Himalaya, this often leads to challenges in accurately representing local conditions (Mukherjee et al., 2025). Strengthening climate observations and promoting data sharing in such regions are essential to improve the accuracy of climate–mass balance relationships, enhance the reliability of future mass balance projections, and support informed policy decisions for sustainable water management. Despite these uncertainties, the overall trend highlights a critical concern: without immediate and effective mitigation efforts, glaciers in the region are likely to undergo significant degradation, threatening downstream water availability, ecological stability, and long-term sustainability.

## 7. Conclusions

This multi-decadal assessment of glacier change in Lahaul–Spiti reveals a persistent and accelerating pattern of glacier retreat and mass loss since the 1970s, with a marked intensification after the early 2000s. By combining multi-temporal geodetic observations with climate datasets, we capture both the spatial heterogeneity and temporal evolution of glacier response, showing that mass loss is neither uniform across glaciers nor constant through time. The acceleration in ice loss coincides with sustained summer and annual temperature rise, warmer transitional seasons, and marginally increasing or declining winter precipitation—conditions that collectively extend the ablation season and intensify melt, even when summer precipitation increases.

The sensitivity of glacier mass balance to summer temperature (−0.49 m w.e. $a^{-1}$ °$C^{-1}$) closely matches with Chhota Shigri Glacier and falls within the range reported for other High Mountain Asia sites. Precipitation exerts a comparatively weaker influence unless significant winter snow accumulation occurs, underscoring the dominant role of temperature in this transitional climatic zone. Projections suggest that, even under the most optimistic emission pathway, the region could lose nearly 70 % of its glacier volume by 2100, with small, low-volume glaciers disappearing well before mid-century. Under intermediate- to high-emission scenarios, losses could exceed half the current volume, threatening downstream hydrology, ecosystems, and socio-economic stability.

A central outcome of this work is the demonstrated value of long-term geodetic measurements as a practical, scalable, and reliable means of quantifying regional geodetic mass balance sensitivity in environments where in-situ data are scarce due to cost and logistical constraints. Unlike single-epoch or short-term studies, sustained geodetic time series reveal critical inter-annual variability and periods of acceleration or slowdown, improving both scientific understanding and model calibration. They provide a cost-effective bridge between sparse field measurements and the need for continuous, large-scale glacier monitoring.

In summary, long-term geodetic observations offer an indispensable pathway to understanding glacier–climate interactions in data-limited mountain regions. They enable accurate reconstructions of past changes, sharpen predictions of future glacier evolution, and inform adaptation strategies for communities reliant on glacier-fed water resources. The evidence here underscores that without such sustained monitoring, both scientific insight and climate resilience planning risk being compromised, particularly in one of the most climate-sensitive regions of the Indian Himalaya. Looking forward, further integrating such geodetic datasets into coordinated global initiatives like the World Glacier Monitoring Service (WGMS) and IPCC assessment frameworks will not only enhance the robustness of climate models but also strengthen the scientific foundation for transboundary water policy, disaster preparedness, and sustainable mountain development strategies.

## CRediT authorship contribution statement

**Atanu Bhattacharya:** Writing – review & editing, Writing – original draft, Visualization, Validation, Supervision, Software, Resources, Project administration, Methodology, Investigation, Funding acquisition, Formal analysis, Data curation, Conceptualization. **Ankita Paul:** Writing – original draft, Methodology, Investigation, Formal analysis. **Kriti Mukherjee:** Writing – review & editing, Writing – original draft, Visualization, Validation, Supervision, Methodology, Investigation, Formal analysis, Conceptualization. **Julekha Khatun:** Methodology, Investigation, Formal analysis. **Sajid Ghuffar:** Validation, Methodology, Formal analysis. **Tobias Bolch:** Writing – review & editing, Supervision, Methodology, Conceptualization.

## Declaration of Generative AI and AI-assisted technologies in the writing process

During the preparation of this work the author(s) used chatgpt in order to refine the language in certain places. After using this tool, the author(s) reviewed and edited the content as needed and take full responsibility for the content of the published article.

## Funding

AB acknowledge the research funding (CRG/2021/002450) received from Anusandhan National Research Foundation (ANRF), Department of Science & Technology (DST), India, under Core Research Grant (CRG); and Ministry of Earth Sciences (MoES), India (MoES/INDO-SWISS/4/2022-PC-I). AP acknowledge the research funding (File no.

DST/WISE-PhD/EA/2024/43) received from Women in Science and Engineering Fellowship for Ph.D. (WISE-PhD) under WISE-KIRAN Division, Department of Science & Technology (DST), Ministry of Science and Technology, Govt. of India.

## Declaration of competing interest

The authors declare that they have no known competing financial interests that could have appeared to influence the work reported in this paper.

### *Acknowledgement*

We acknowledge the partners of DINAMIS (French National Facility for Shared Access to Very High-Resolution Satellite Imagery), part of the research infrastructure Data Terra, for facilitating the acquisition of Pleiades imagery and the Pléiades Glacier Observatory (PGO). We are grateful to the satellite data providers: USGS for Carona KH4, Hexagon KH9, Landsat (https://earthexplorer.usgs.gov/); JPL/NASA and METI for ASTER L1A (https://urs.earthdata.nasa.gov/); National Remote Sensing Center (NRSC), India, for providing Cartosat-1 raw stereo data (https://bhoonidhi.nrsc.gov.in/bhoonidhi/home.html); Open Topography for NASA DEM (https://opentopography.org/); India Meteorological Department (IMD), India, for weather station data; Climate Explorer for climate data based on Phase 6 of the Coupled Model Intercomparison Project (CMIP6) (https://climexp.knmi.nl/); Copernicus for The ERA5 Land reanalysis data (https://climate.copernicus.eu/climate-reanalysis); GLIMS for glacier outlines (https://www.glims.org/RGI/randolph70.html).

## Appendix A. Supplementary data

Supplementary data to this article can be found online at https://doi.org/10.1016/j.scitotenv.2025.181261.

## Data availability

All satellite data which is not restricted by license agreements (e.g. the original satellite) will be made available to the international community through the MountCryo (www.mountcryo.org/dataset/) data portal.

## References

Allen, S.K., Zhang, G., Wang, W., Yao, T., Bolch, T., 2019. Potentially dangerous glacial lakes across the Tibetan plateau revealed using a large-scale automated assessment approach. Sci. Bull. 64, 435–445. https://doi.org/10.1016/j.scib.2019.03.011.

Azam, M.F., Vincent, C., Srivastava, S., Berthier, E., Wagnon, P., Kaushik, H., Hussain, A., Munda, M.K., Mandal, A., Ramanathan, A., 2024. Reanalysis of the longest mass balance series in Himalaya using a nonlinear model: Chhota Shigri glacier (India). Cryosphere 18, 5653–5672. https://doi.org/10.5194/tc-18-5653-2024.

Azam, M.F., Wagnon, P., Vincent, C., Ramanathan, A.L., Favier, V., Mandal, A., Pottakkal, J.G., 2014. Processes governing the mass balance of Chhota Shigri glacier (western Himalaya, India) assessed by point-scale surface energy balance measurements. Cryosphere 8 (6), 2195–2217. https://doi.org/10.5194/tc-8-2195-2014.

Azam, M.F., Wagnon, P., Ramanathan, A., Vincent, C., Sharma, P., Arnaud, Y., Linda, A., Pottakkal, J.G., Chevallier, P., Singh, V.B., Berthier, E., 2012. From balance to imbalance: a shift in the dynamic behaviour of Chhota Shigri glacier, western Himalaya, India. J. Glaciol. 58 (208), 315–324. https://doi.org/10.3189/2012JoG11J123.

Berthier, E., Lebreton, J., Fontannaz, D., Hosford, S., Belart, J.M.C., Brun, F., Andreassen, L.M., Menounos, B., Blondel, C., 2024. The Pléiades glacier observatory: high-resolution digital elevation models and ortho-imagery to monitor glacier change. Cryosphere 18 (12), 5551–5571. https://doi.org/10.5194/egusphere-2024-250.

Bhattacharya, A., Bolch, T., Mukherjee, K., King, O., Menounos, B., Kapitsa, V., Neckel, N., Yang, W., Yao, T., 2021. High Mountain Asian glacier response to climate revealed by multi-temporal satellite observations since the 1960s. Nat. Commun. 12, 4133. https://doi.org/10.1038/s41467-021-24180-y.

Bhattacharya, A., Mukherjee, K., King, O., Karmakar, S., Remya, S.N., Kulkarni, A.V., Kropáček, J., Bolch, T., 2023. Influence of climate and non-climatic attributes on declining glacier mass budget and surging in Alaknanda Basin and its surroundings. Glob. Planet. Chang. 230, 104260. https://doi.org/10.1016/j.gloplacha.2023.104260.

Bolch, T., Kulkarni, A., Kaab, A., Huggel, C., Paul, F., Cogley, J.G., Frey, H., Kargel, J.S., Fujita, K., Scheel, M., Bajracharya, S., Stoffel, M., 2012. The state and fate of Himalayan glaciers. Science 336 (6079), 310–314. https://doi.org/10.1126/science.1215828.

Bolch, T., Menounos, B., Wheate, R., 2010. Landsat-based inventory of glaciers in western Canada, 1985–2005. Remote Sens. Environ. 114, 127–137. https://doi.org/10.1016/j.rse.2009.08.015.

Bolch, T., Pieczonka, T., Benn, D.I., 2011. Multi-decadal mass loss of glaciers in the Everest area (Nepal Himalaya) derived from stereo imagery. Cryosphere 5, 349–358. https://doi.org/10.5194/tc-5-349-2011.

Brock, B.W., Mihalcea, C., Kirkbride, M.P., Diolaiuti, G., Cutler, M.E.J., Smiraglia, C., 2010. Meteorology and surface energy fluxes in the 2005–2007 ablation seasons at the Miage debris-covered glacier, Mont Blanc massif, Italian Alps. J. Geophys. Res. Atmos. 112 (D9). https://doi.org/10.1029/2009JD013224.

Brun, F., Berthier, E., Wagnon, P., Kääb, A., Treichler, D., 2017. A spatially resolved estimate of High Mountain Asia glacier mass balances from 2000 to 2016. Nat. Geosci. 10, 668–673. https://doi.org/10.1038/ngeo2999.

Collins, M., Chandler, R.E., Cox, P.M., Huthnance, J.M., Rougier, J., Stephenson, D.B., 2012. Quantifying future climate change. Climate Change 2 (6), 403–409. https://doi.org/10.1038/nclimate1414.

Dimri, A.P., Yasunari, T., Wiltshire, A., Kumar, P., Mathison, C., Ridley, J., Jacob, D., 2013. Application of regional climate models to the Indian winter monsoon over the western Himalayas. Sci. Total Environ. 468-469, S36–S47. https://doi.org/10.1016/j.scitotenv.2012.04.011.

Engelhardt, M., Schuler, T.V., Andreassen, L.M., 2015. Sensitivities of glacier mass balance and runoff to climate perturbations in Norway. Ann. Glaciol. 56 (70), 79–88. https://doi.org/10.3189/2015AoG70A004.

Eyring, V., Bony, S., Meehl, G.A., Senior, C.A., Stevens, B., Stouffer, R.J., Taylor, K.E., 2016. Overview of the coupled model Intercomparison project phase 6 (CMIP6) experimental design and organization. Geosci. Model Dev. 9 (5), 1937–1958. https://doi.org/10.5194/gmd-9-1937-2016.

Falaschi, D., Bhattacharya, A., Guillet, G., Huang, L., King, O., Mukherjee, K., Rastner, P., Yao, T., Bolch, T., 2023. Annual to seasonal glacier mass balance in High Mountain Asia derived from Pléiades stereo images: examples from the Pamir and the Tibetan plateau. Cryosphere 17 (12), 5435–5458. https://doi.org/10.5194/tc-17-5435-2023.

Farinotti, D., Huss, M., Fürst, J.J., Landmann, J., Machguth, H., Maussion, F., Pandit, A., 2019. A consensus estimate for the ice thickness distribution of all glaciers on earth. Nat. Geosci. 12 (3), 168–173. https://doi.org/10.1038/s41561-019-0300-3.

Gardelle, J., Berthier, E., Arnaud, Y., Kääb, A., 2013. Region-wide glacier mass balances over the Pamir-Karakoram-Himalaya during 1999–2011. Cryosphere 7 (4), 1263–1286. https://doi.org/10.5194/tc-7-1263-2013.

Garg, P.K., Shukla, A., Tiwari, R.K., Jasrotia, A.S., 2017. Assessing the status of glaciers in part of the Chandra basin, Himachal Himalaya: a multiparametric approach. Geomorphology 284, 99–114. https://doi.org/10.1016/j.geomorph.2016.10.022.

Ghuffar, S., Bolch, T., Rupnik, E., Bhattacharya, A., 2022. A pipeline for automated processing of declassified Corona KH-4 (1962–1972) stereo imagery. IEEE Transactions on Geosciences and Remote Sensing. 60, 1–14. https://doi.org/10.1109/TGRS.2022.3200151.

Ghuffar, S., King, O., Guillet, G., Rupnik, E., Bolch, T., 2023. Brief communication: glacier mapping and change estimation using very high-resolution declassified hexagon KH-9 panoramic stereo imagery (1971–1984). Cryosphere 17 (3), 1299–1306. https://doi.org/10.5194/tc-17-1299-2023.

GlaMBIE Team, 2025. Community estimate of global glacier mass changes from 2000 to 2023. Nature 639, 382–388. https://doi.org/10.1038/s41586-024-08545-z.

Hall, D.K., Bayr, K.J., Schöner, W., Bindschadlerd, R.A., Chiene, J.Y.L., 2003. Consideration of the errors 823 inherent in mapping historical glacier positions in Austria from the ground and space (1893–2001). Remote Sens. Environ. 86, 566–577. https://doi.org/10.1016/S0034-4257(03)00134-2.

Hock, R., Bliss, A., Marzeion, B.E., Giesen, R.H., Hirabayashi, Y., Huss, M., Radić, V., Slangen, A.B., 2019. GlacierMIP–A model intercomparison of global-scale glacier mass-balance models and projections. J. Glaciol. 65 (251), 453–467. https://doi.org/10.1017/jog.2019.22.

Hock, R., Huss, M., 2021. Glaciers and climate change. In: Climate Change, pp. 157–176. https://doi.org/10.1016/B978-0-12-821575-3.00009-8.

Hugonnet, R., McNabb, R., Berthier, E., Menounos, B., Nuth, C., Girod, L., Daniel, F., Matthias, H., Dussaillant, I., Brun, F., Kääb, A., 2021. Accelerated global glacier mass loss in the early twenty-first century. Nature 592, 726–731. https://doi.org/10.1038/s41586-021-03436-z.

Huss, M., 2013. Density assumptions for converting geodetic glacier volume change to mass change. Cryosphere 7 (3), 877–887. https://doi.org/10.5194/tc-7-877-2013.

Huss, M., Hock, R., 2018. Global-scale hydrological response to future glacier mass loss. Nat. Clim. Chang. 8, 135–140. https://doi.org/10.1038/s41558-017-0049-x.

Immerzeel, W.W., Lutz, A.F., Andrade, M., Bahl, A., Biemans, H., Bolch, T., Hyde, S., Brumby, S., Davis, B.J., Elmore, A.C., Emmer, A., Feng, M., Fernandez, A., Haritashya, U., Kargel, J.S., Koppes, M., Kraaijenbrink, P.D.A., Kulkarni, A.V., Mayewski, P.A., Nepal, S., Pacheco, P., Painter, T.H., Pellicciotti, F., Rajaram, H., Rupper, S., Sinisolo, A., Shrestha, A.B., Viviroli, D., Wada, Y., Xiao, C., Yao, T., Baillie, J.E.M., 2020. Importance and vulnerability of the world's water towers. Nature 577, 364–369. https://doi.org/10.1038/s41586-019-1822-y.

Kääb, A., Berthier, E., Nuth, C., Gardelle, J., Arnaud, Y., 2012. Contrasting patterns of early twenty-first-century glacier mass change in the Himalayas. Nature 488, 495–498. https://doi.org/10.1038/nature11324.

Kulkarni, A.V., Rathore, B.P., Singh, S.K., Bahuguna, I.M., 2011. Understanding changes in the Himalayan cryosphere using remote sensing techniques. Int. J. Remote Sens. 32 (3), 601–615. https://doi.org/10.1080/01431161.2010.517802.

Kulkarni, A.V., Dhar, S., Rathore, B.P., Raj, K, Kalia, R., 2006. Recession of samudra tapu glacier, chandra river basin, Himachal Pradesh. J. Indian. Soc. Remote. Sens. 34, 39–46. https://doi.org/10.1007/BF02990745.

Laha, S., Kumari, R., Singh, S., Mishra, A., Sharma, T., Banerjee, A., Nainwal, H.C., Shankar, R., 2017. Evaluating the contribution of avalanching to the mass balance of Himalayan glaciers. Ann. Glaciol. 58, 110–118. https://doi.org/10.1017/aog.2017.27.

Matthews, T., Perry, L.B., Aryal, D., Elmore, A.C., Khadka, A., Pelto, M., Shrestha, D., Wilby, R., 2021. Weather on K2 during historic first winter ascent. Weather 77 (2), 49–52. https://doi.org/10.1002/wea.4094.

Maurer, J.M., Scheafer, J.M., Rupper, S., Korley, A., 2019. Acceleration of ice loss across the Himalayas over the past 40 years. Sci. Adv. 5, 6. https://doi.org/10.1126/sciadv.aav7266.

McNabb, R., Nuth, C., Kääb, A., Girod, L., 2019. Sensitivity of glacier volume change estimation to DEM void interpolation. Cryosphere 13 (3), 895–910. https://doi.org/10.5194/tc-13-895-2019.

Miles, E., McCarthy, M., Dehecq, A., Kneib, M., Fugger, S., Pellicciotti, F., 2021. Health and sustainability of glaciers in High Mountain Asia. Nat. Commun. 12 (1), 2868. https://doi.org/10.1038/s41467-021-23073-4.

Mukherjee, K., Bhattacharya, A., Ghuffar, S., King, O., Paul, A., Bolch, T., Menounos, B., 2025. Variabilities in climate sensitivities and mass balance of four High Mountain Asian glaciers. Glob. Planet. Chang. 255, 105044. https://doi.org/10.1016/j.gloplacha.2025.102044.

Mukherjee, K., Bhattacharya, A., Pieczonka, T., Ghosh, S., Bolch, T., 2018. Glacier mass budget and climate reanalysis data indicate a climatic shift around 2000 in Lahaul-Spiti, western Himalaya. Climate Change 148, 219–233. https://doi.org/10.1007/s10584-018-2185-3.

Muñoz-Sabater, J., Dutra, E., Agustí-Panareda, A., Albergel, C., Arduini, G., Balsamo, G., Boussetta, S., Choulga, M., Harrigan, S., Hersbach, H., Martens, B., Miralles, D.G., Piles, M., Rodríguez-Fernández, N.J., Zsoter, E., Buontempo, C., Thépaut, J.N., 2021. ERA5-Land: a state-of-the-art global reanalysis dataset for land applications. Earth. Syst. Sci. Data 13 (9), 4349–4383. https://doi.org/10.5194/essd-13-4349-2021.

Nuth, C., Kääb, A., 2011. Co-registration and bias corrections of satellite elevation data sets for quantifying glacier thickness change. Cryosphere 5 (1), 271–290. https://doi.org/10.5194/tc-5-271-2011.

Oerlemans, J., Anderson, B., Hubbard, A., Huybrechts, P., Johannesson, T., Knap, W.H., Schmeits, M., Stroeven, A.P., Van de Wal, R.S.W., Wallinga, J., Zuo, Z., 1998. Modelling the response of glaciers to climate warming. Clim. Dyn. 14, 267–274. https://doi.org/10.1007/s003820050222.

Pandey, P., Venkataraman, G., 2013. Changes in the glaciers of Chandra–Bhaga basin, Himachal Himalaya, India, between 1980 and 2010 measured using remote sensing. Int. J. Remote Sens. 34 (15), 5584–5597. https://doi.org/10.1080/01431161.2013.793464.

Patel, L.K., Sharma, A., Sharma, P., Singh, A., Thamban, M., 2021. Glacier area changes and its relation to climatological trends over Western Himalaya between 1971 and 2018. J. Earth. Syst. Sci. 130, 217. https://doi.org/10.1007/s12040-021-01720-0.

Pieczonka, T., Bolch, T., 2015. Region-wide glacier mass budgets and area changes for the central Tien Shan between~ 1975 and 1999 using hexagon KH-9 imagery. Glob. Planet. Chang. 128, 1–13. https://doi.org/10.1016/j.gloplacha.2014.11.014.

Ramsankaran, R., Pandit, A., Parla, A., 2019. Decadal estimates of surface mass balance for glaciers in Chandra Basin, Western Himalayas, India—A geodetic approach. In: Venkataraman, C., Mishra, T., Ghosh, S., Karmakar, S. (Eds.), Climate Change Signals and Response. Springer, Singapore. https://doi.org/10.1007/978-981-13-0280-0_7.

Rasmussen, L.A., 2013. Meteorological controls on glacier mass balance in High Asia. Ann. Glaciol. 54 (63), 352–359. https://doi.org/10.3189/2013AoG63A353.

Rasmussen, R., Baker, B., Kochendorfer, J., Myers, T., Landolt, S., Fisher, A., Black, J., Theriault, J., Kucera, P., Gochis, D., Smith, C., 2012. The NOAA/FAA/NCAR winter precipitation test bed: how well are we measuring snow. Bull. Am. Meteorol. Soc. 93, 811–829. https://doi.org/10.1175/BAMS-D-11-00052.1.

RGI v7.0 Consortium, 2023. Randolph Glacier Inventory - A Dataset of Global Glacier Outlines, Version 7.0. Boulder, Colorado USA. NSIDC: National Snow and Ice Data Center. doi:https://doi.org/10.5067/f6jmovy5navz. Online access: doi: https://doi.org/10.5067/f6jmovy5navz.

Rolstad, C., Haug, T., Denby, B., 2009. Patially integrated geodetic glacier mass balance and its uncertainty based on geostatistical analysis: application to the western Svartisen ice cap, Norway. J. Glaciol. 55 (192), 666–680. https://doi.org/10.3189/002214309789470950.

Rounce, D.R., Hock, R., Hugonnet, R., Kochtitzky, W., Huss, M., Berthier, E., Brinkerhoff, D., Compagno, L., Copland, L., Farinotti, D., Menounos, B., McNabb, R. W., 2023. Global glacier change in the 21st century: every increase in temperature matters. Science 379 (6627), 78–83. https://doi.org/10.1126/science.abo1324.

Rounce, D.R., Hock, R., McNabb, R.W., Millan, R., Sommer, C., Braun, M.H., Malz, P., Maussion, F., Mouginot, J., Seehaus, T.C., Shean, D.E., 2021. Distributed global debris thickness estimates reveal debris significantly impacts glacier mass balance. Geophys. Res. Lett. 48 (8), e2020GL091311. https://doi.org/10.1029/2020GL091311.

Sahu, R., Gupta, R.D., 2020. Glacier mapping and change analysis in Chandra basin, Western Himalaya, India during 1971–2016. Int. J. Remote Sens. 41 (18), 6914–6945. https://doi.org/10.1080/01431161.2020.1752412.

Sahu, R., Singh, D.P., Sonker, D., Rai, S., 2024, December. Glacier change analysis of glaciers in Chandra basin, Western Himalaya during 1965–2023. In: 2024 IEEE India Geoscience and Remote Sensing Symposium (InGARSS), pp. 1–4. https://doi.org/10.1109/InGARSS61818.2024.11105092.

Sakai, A., Fujita, K., 2017. Contrasting glacier responses to recent climate change in high-mountain Asia. Sci. Rep. 7 (1), 13717. https://doi.org/10.1038/s41598-017-14256-5.

Shean, D.E., Alexandrov, O., Moratto, Z.M., Smith, B.E., Joughin, I.R., Porter, C., Morin, P., 2016. An automated, open-source pipeline for mass production of digital elevation models (DEMs) from very-high-resolution commercial stereo satellite imagery. ISPRS J. Photogramm. Remote Sens. 116, 101–117. https://doi.org/10.1016/j.isprsjprs.2016.03.012.

Silverman, N.L., Maneta, M.P., 2016. Detectability of change in winter precipitation within mountain landscapes: spatial patterns and uncertainty. Water Resour. Res. 52 (6), 4301–4320. https://doi.org/10.1002/2014WR016493.

Sun, F., Roderick, M.L., Farquhar, G.D., 2018. Rainfall statistics, stationarity, and climate change. Proc. Natl. Acad. Sci. 115 (10), 2305–2310. https://doi.org/10.1073/pnas.1705349115.

Tawde, S.A., Kulkarni, A.V., Bala, G., 2017. An estimate of glacier mass balance for the Chandra basin, western Himalaya, for the period 1984–2012. Ann. Glaciol. 58 (75), 99–109. https://doi.org/10.1017/aog.2017.18.

Vatsal, S., Azam, M.F., Bhardwaj, A., Mandal, A., Bahuguna, I., Ramanathan, A., Raju, N. J., Tomar, S.S., 2024. Glacier area change (1993–2019) and its relationship to debris cover, proglacial lakes, and morphological parameters in the Chandra-Bhaga Basin, Western Himalaya, India. J. Mt. Sci. 21, 1287–1306. https://doi.org/10.1007/s11629-023-8277-1.

Vijay, S., Braun, M., 2016. Elevation change rates of glaciers in the Lahaul-Spiti (Western Himalaya, India) during 2000–2012 and 2012–2013. Remote Sens. 8 (12), 1038. https://doi.org/10.3390/rs8121038.

Vincent, C., Ramanathan, A., Wagnon, P., Dobhal, D.P., Linda, A., Berthier, E., Sharma, P., Arnaud, Y., Azam, M.F., Gardelle, J., 2013. Balanced conditions or slight mass gain of glaciers in the Lahaul and Spiti region (northern India, Himalaya) during the nineties preceded recent mass loss. Cryosphere 7 (2), 569–582. https://doi.org/10.5194/tc-7-569-2013.

Wang, R., Liu, S., Shangguan, D., Radić, V., Zhang, Y., 2019. Spatial heterogeneity in glacier mass-balance sensitivity across High Mountain Asia. Water 11 (4), 776. https://doi.org/10.3390/w11040776.

Wang, T., Zhao, Y., Xu, C., Ciais, P., Liu, D., Yang, H., Piao, S., Yao, T., 2021. Atmospheric dynamic constraints on Tibetan plateau freshwater under Paris climate targets. Nat. Clim. Chang. 11 (3), 219–225. https://doi.org/10.1016/j.atmosres.2022.106494.

WGMS, 2024. Fluctuations of Glaciers Database. World Glacier Monitoring Service (WGMS). Zurich, Switzerland. https://doi.org/10.5904/wgms-fog-2024-01.

Zhu, Y.Y., Yang, S., 2020. Evaluation of CMIP6 historical temperature and precipitation over the Tibetan plateau and its comparison with CMIP5. Adv. Clim. Chang. Res. 11 (3), 239–251. https://doi.org/10.1016/j.atmosres.2020.105099.

https://dspace.org/

# Multi-decadal geodetic mass balance, climate sensitivity, and projected glacier response in the Chandra–Bhaga Basin, Western Indian Himalaya (1971–2100)

**Bhattacharya, Atanu; Paul, Ankita; Mukherjee, Kriti; Khatun, Julekha; Ghuffar, Sajid ...**

**2026-02-01**
Elsevier
https://doi.org/10.1016/j.scitotenv.2025.181261
Bhattacharya A, Paul A, Mukherjee K, et al., (2026) Multi-decadal geodetic mass balance, climate sensitivity, and projected glacier response in the Chandra–Bhaga Basin, Western Indian Himalaya (1971–2100). Science of The Total Environment, Volume 1014, February 2026, Article number 181261

Downloaded from a DSpace repository. https://dspace.org/